

The thermal evolution of planetesimals during accretion and differentiation: consequences for dynamo generation by thermally-driven convection.

K.H. Dodds¹, J.F.J. Bryson², J.A. Neufeld^{1,3,4} and R.J. Harrison¹

¹Department of Earth Sciences, University of Cambridge, Cambridge, UK

²Department of Earth Sciences, University of Oxford, Oxford, UK

³BP Institute, University of Cambridge, Cambridge, UK

⁴Department of Applied Mathematics and Theoretical Physics, University of Cambridge, Cambridge, UK

Key Points:

- Partitioning of ^{26}Al into asteroids' mantles led to the growth of a thermally stratified layer in the core
- Gradual accretion prevents this stratification from developing and enables dynamo generation
- The timing and duration of thermal dynamo fields provide constraints on accretionary history

Corresponding author: Kathryn Dodds, khd23@cam.ac.uk

Abstract

The meteorite paleomagnetic record indicates that differentiated (and potentially, partially differentiated) planetesimals generated dynamo fields in the first 6-20 Myr after the formation of calcium-aluminium-rich inclusions (CAIs). This early period of dynamo activity has been attributed to thermal convection in the liquid cores of these planetesimals during an early period of magma ocean convection. To better understand the controls on thermal dynamo generation in planetesimals, we have developed a 1D model of the thermal evolution of planetesimals from accretion through to the shutoff of convection in their silicate magma oceans for a variety of accretionary scenarios. The heat source of these bodies is the short-lived radiogenic isotope, ^{26}Al . During differentiation, ^{26}Al partitions into the silicate portion of these bodies, causing their magma ocean to heat up and introducing stable thermal stratifications to the tops of their cores, which inhibits dynamo generation. In ‘instantaneously’ accreting bodies, this effect causes a delay on the order of > 10 Myr to whole core convection and dynamo generation while this stratification is eroded. However, gradual core formation in bodies that accrete over > 0.1 Myr can minimise the development of this stratification, allowing dynamo generation from ~ 4 Myr after CAI formation. Our model also predicts partially differentiated planetesimals with a core and mantle overlain by a chondritic crust for accretion timescales > 1.2 Myr, although none of these bodies generate a thermal dynamo field. We compare our results from thousands of model runs to the meteorite paleomagnetic record to constrain the physical properties of their parent bodies.

Plain Language Summary

The meteorite paleomagnetic record shows that magnetic field generation within the liquid cores of their parent asteroids was widespread during the first 200 million years of our solar system. These bodies, termed planetesimals, formed during the first few million years of the solar system and were the building blocks of the terrestrial planets and cores of the gas giants. However, it can be difficult to determine the physical properties (such as size) of these planetesimals from the meteorites themselves. Magnetic field generation in a liquid iron core places constraints on the size of these early planetary bodies as well as requirements on how fast they were cooling. In this study, we have modelled the thermal evolution of a number of planetesimals and recorded when they were able to generate a magnetic field. We find that the timing and duration of magnetic field generation depends strongly on the timescale of accretion and size of the planetesimal.

1 Introduction

Advances in rock magnetism and paleomagnetic techniques over the past two decades have revealed that many meteorites carry primary magnetic remanences imparted by magnetic fields generated in the first few 100 Myr after the formation of the solar system. This primary remanence has been found in both achondrites (e.g. Fu et al. (2012), Bryson et al. (2015), Wang et al. (2017)), which sample the mantles of differentiated planetesimals, as well as chondritic meteorites (e.g. Carporzen et al. (2011), Cournede et al. (2015), Gattacceca et al. (2016), Shah et al. (2017), Bryson et al. (2019a), Cournède et al. (2020), Maurel et al. (2020)), which are usually considered to be samples of unmelted, undifferentiated planetesimals. The potential candidates for the source of these magnetic fields in the early solar system include the nebular field generated by the protoplanetary disk itself, dynamo fields produced in the liquid or semi-liquid core of planetesimals, shock fields from impacts between planetary bodies and the solar wind field. The possibility of the solar wind being the source of the magnetisation in the meteorites has been discounted largely due to the low field intensity of the solar wind field in the planet-forming regions of the solar system compared to the recovered paleointensities of the meteorites (Oran et al., 2018).

Short-lived radioisotope systems have been used to constrain the timing of the primary remanence acquired either as the host meteorite cooled, imparting a thermoremanent magnetisation (TRM), or was aqueously altered, leading to the generation of new magnetic minerals that record a chemical transformation remanent magnetisation (CTRM) as they grew. Combined with the paleointensities recovered from these meteorites, these ages provide a picture of the evolution of magnetic fields generated by asteroids during the early solar system is emerging (Figure 1). This record can be split into five epochs: three during which magnetic fields were active and two with very weak or null fields. The first episode of magnetic field generation was from $\sim 0-4$ Myr after the formation of the solar system 4567.3 Myr ago (Connelly et al., 2012) where the age of the solar system is taken as the age of the first condensate solids to form, calcium-aluminium inclusions (CAIs). There was then a pause in magnetic field generation between ~ 4 and 6 Myr after CAI formation (Gattacceca et al., 2016, Wang et al., 2017, Weiss et al., 2017). The second recorded period of magnetism was from $\sim 6-20$ Myr after CAI formation, which was followed by a pause in magnetic activity from $\sim 20-65$ Myr after CAI formation.

The final episode of magnetic field generation in planetesimals was from $\sim 65\text{--}250$ Myr after CAI formation.

The earliest period (from the start of the solar system to ~ 4 Myr after CAI formation) has been attributed to the nebular magnetic field generated by the protoplanetary disk around the young Sun (Fu et al., 2014a, Fu et al., 2020). It has been argued that dynamo field generation in planetesimals was not possible at this time due to the partitioning of the short lived radioisotope ^{26}Al , which has a half-life of 0.717 Myr (Neumann et al., 2014), into the silicate portion of the body on differentiation (Bryson et al., 2019a). This leads to a period during which planetesimals' mantles are hotter than their cores which prevents core convection and dynamo generation. Bryson et al. (2019a) suggests that it takes up to 5.5 Myr after CAI formation for the supply of the heat source ^{26}Al to be sufficiently depleted to allow mantle and subsequent core cooling. This leads to a delay in dynamo generation until 5.5 Myr after CAI formation, by which time the solar nebula and its associated magnetic field had dissipated (Wang et al., 2017).

The latter two periods of early Solar System magnetism have been linked to dynamo generation within the (semi-)fluid cores of the meteorite parent bodies (e.g. Elkins-Tanton, Weiss, & Zuber, 2011). The ability for a planetary body to generate a core dynamo field places stringent constraints on the internal heat transfer occurring at that time. As such, the timing and duration of these early fields has been used to infer properties of meteorites parent bodies such as their size and accretion timing (Elkins-Tanton et al., 2011, Bryson, Neufeld, & Nimmo, 2019b). The period of magnetism from $\sim 6\text{--}20$ Myr after CAI formation has been attributed to dynamo fields driven by relatively rapid core cooling with no core crystallisation. This is an inefficient method of dynamo generation as the density difference induced by core cooling is orders of magnitude lower than that created during core solidification and requires core cooling rates of $> 1\text{K Myr}^{-1}$ in cores of > 200 km in radius (Nimmo, 2009). Such fast cooling rates are only possible in the first few tens of Myr after the formation of solar system when these small bodies lose heat from their surfaces through semi-molten convecting magma oceans in their interiors (Elkins-Tanton et al., 2011, Sterenborg & Crowley, 2013, Bryson et al., 2019b). Once convection in the silicate portion of the body ceases, the body cools more slowly by conduction which leads to subadiabatic core heat fluxes and no core convection.

The youngest period of magnetism from $\sim 65 - 250$ Myr after solar system formation has been linked to dynamo fields generated during core crystallisation on the parent bodies (Bryson et al., 2015, Bryson et al., 2019a and Maurel et al., 2020). The exact mode of core crystallisation in planetesimals is uncertain and may proceed from a nucleus outward (as with the Earth’s inner core) or inwards from the core-mantle boundary (CMB), depending predominantly on the size of core and its light element content (Williams, 2009). As such, the potential mechanisms of dynamo generation during core solidification are uncertain. If the core solidifies outwardly, these bodies could generate a dynamo through the same mechanism as the Earth by convection driven primarily by the expulsion of light elements at the inner core boundary. However, if the core starts crystallising inwardly from the CMB, dynamo generation cannot be generated directly by the rejection of light elements from the advancing solid. Instead, it has been proposed that dynamo activity could have been powered by the remelting of solid ‘iron snow’ as it falls into the interior of the core, as has been proposed for Ganymede (Rückriemen et al., 2015), or driven by the delamination of solidified iron from the CMB, as proposed for the IVA meteorite parent body (Neufeld et al., 2019). The timing and durations of any late-stage fields produced will depend on the dynamo generation mechanism, which depends on the mode and direction of solidification, and the resultant thermal and compositional stratification as this controls the fluid density and hence the drive for vigorous convection. The sulfur concentration of the core is critical to this as this element has a strong influence on the liquidus temperature of Fe-FeS alloys with pure Fe melting at 1810 K and eutectic Fe-FeS at 1234 K (Sternborg & Crowley, 2013).

In this study, we aim to elucidate the first period of magnetic field generation in asteroid-sized bodies from $\sim 6 - 20$ Myr after CAI formation that has been linked to dynamos created by thermal convection in planetesimal cores alone. The ability for asteroid-sized bodies to generate thermally-driven dynamos depends on both the rate at which their cores cool and the distance over which their core convects. However, whether a core is able to convect during this period is uncertain for the following reason. Differentiation in these bodies is driven by the decay of the short-lived radioisotope, ^{26}Al , which partitions into the silicate mantle during core formation. This is expected to lead to a period during which the mantle becomes hotter than the core due to the continued decay of ^{26}Al while internal heating is absent in the core. The diffusion of heat from the magma ocean into the top of the core will lead to the development of a stable thermal

stratification in the core. Once the core starts to cool, this stable thermal stratification will inhibit core convection and thus dynamo generation. The duration and mechanism of core formation is therefore important as it will control the extent to which this stable stratification develops. Previous studies that investigate the possibility of thermally driven dynamo generation in planetesimals such as Elkins-Tanton et al. (2011) and Bryson et al. (2019b) assume core formation is instantaneous and do not explicitly model the build up and subsequent decay of any thermal stratification in the core. We include these core formation processes in our models to better constrain the effects of accretion and the mechanism of core formation on thermally driven dynamo generation and improve our understanding of what the timing and duration of these early fields can tell us about the thermal and accretionary history of planetesimals.

We do this by building a 1D model of a planetesimal’s thermal and structural evolution during accretion, differentiation and magma ocean convection. We then use existing scaling laws to convert the predicted heat flux out of the core to a magnetic Reynolds number, which we use to predict whether a core is capable of generating a dynamo field. This is a similar approach as that taken by Elkins-Tanton et al. (2011), Sterenborg and Crowley (2013) and Bryson et al. (2019b). These studies demonstrated that thermally-driven dynamo generation lasting for longer than 10 Myr is possible in large planetesimals. However, the minimum planetary radius required for this varies among these studies with $R_p > 200$ km, Elkins-Tanton et al. (2011); $R_p > 320$ km, Bryson et al. (2019b) and $R_p > 500$ km, Sterenborg and Crowley (2013). We build on these previous studies by including the gradual accretion and differentiation of planetesimals and assess the extent to which these processes affect the thermal structure of the core and hence any ability to generate a thermal dynamo. Moreover the inclusion of this process allows us to constrain the timescale of planetesimal accretion from the properties of the magnetic field it generates for the first time. Gradual accretion of chondrules to the planetesimal’s surface, as described in Johansen et al. (2015), also allows for the development of partially differentiated planetesimals. We then use our model results to constrain the accretionary history of the angrite parent body, which had an active dynamo field at 11 Myr after CAI formation (Wang et al., 2017). Finally, we use the results of our modelling to discuss the paleomagnetic record of early magnetic field generation in planetesimals.

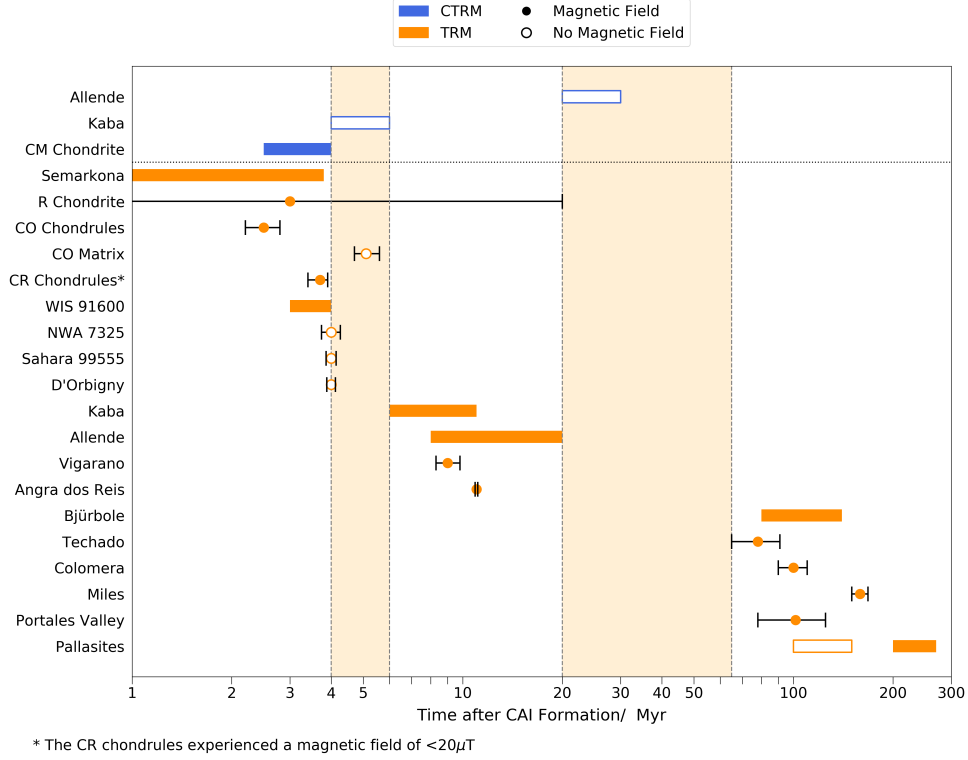


Figure 1. Meteorite Paleomagnetic Record with data from Carporzen et al., 2011, Fu et al., 2014b, Fu et al., 2014a, Cournede et al., 2015, Bryson et al., 2015, Gattacceca et al., 2016, Nichols et al., 2016, Weiss et al., 2017, Shah et al., 2017, Wang et al., 2017, Maurel et al., 2018, Bryson et al., 2019a, Borlina et al., 2020, Fu et al., 2020, Maurel et al., 2020, Cournède et al., 2020 and Bryson et al., 2020. Points represent meteorites where the age of the magnetic remanence has been dated using a geochronometer and the analytical uncertainty on this age is shown by the error bars. Bars represent meteorites where the age of the magnetic remanence is inferred from a separate measurement (e.g., cooling rate). Orange markers correspond to thermoremanent magnetisations (TRMs); blue markers correspond to chemical transformation remnant magnetisations acquired during aqueous alteration (CTRM). Filled markers represent samples where remanence was imparted by a magnetic field $> 2\mu T$. The open markers denote meteorites which experienced a magnetic field $< 2\mu T$ indicating they experienced a weak or null magnetic field. The grey dashed lines separate the periods of presence and absence of magnetic fields in the early Solar System. Whether the R chondrites experienced the early nebula field or an internal dynamo field is uncertain due to the large ± 17 Myr on the age of the remanence. The R chondrites could also have recorded a remanence between 4 – 6 Myr after CAI formation, which would argue against the pause in magnetic field generation in the early solar system recorded by other meteorite groups. The uncertainty on the Pb-Pb age of the angrite, Angra dos Reis, is ± 0.1 Myr (Weiss et al., 2017)

2 Thermal Evolution Model

2.1 Model Overview

Our model considers the thermal evolution of a planetesimal, from accretion and differentiation through to magnetic field generation and the cessation of magma ocean convection. The thermal evolution of these bodies can be split into five stages (Figure 2). In Stage 1, the planetesimal gradually accretes chondritic material to its surface (Johansen et al., 2015) whilst it is heated by the radioactive decay of the short-lived radioisotope, ^{26}Al . This leads to metal melting at ~ 1200 K followed by partial melting of the silicates up to ~ 1600 K. The decrease in viscosity caused by the presence of > 20 wt% silicate melting leads to differentiation and the onset of convection across a portion of the planetesimal. The initiation of this process marks the start of Stage 2 when core formation can commence as shear strains are introduced that create pathways down which the metal melt can flow to the centre of the body. The differentiation into a core and overlying semi-molten magma ocean leads to partitioning of ^{26}Al into the magma ocean and a period during which the magma ocean continues to produce heat and can become hotter than the core. The diffusion of this heat into the core can lead to the development of a stably stratified thermal structure at shallow depths in the core, which can inhibit core convection and dynamo generation. Once the ^{26}Al in the mantle is extinct, the planetesimal begins cooling. This gradually causes any stratification in the core to be removed (Stage 3), leading to convection in the core and the potential for dynamo generation (Stage 4). The model ends with the cessation of convection in the silicate portion of the planetesimal (Stage 5). We predict the timing and duration of any dynamo fields generated by using scaling laws from Olson and Christensen (2006), which relate the superadiabatic heat flux to the magnetic Reynolds number.

Stage 1, which consists of the accretion and initial heating of the planetesimal, is similar to that described in Neumann et al. (2012). However, here we do not model core formation and differentiation using multiphase flow between the silicate and metal melts and solids. Instead, we argue that these processes occurred rapidly after the onset of convection in the planetesimal (Bryson et al., 2019b). The presence of magma oceans on planetesimals has been hotly debated (Wilson & Keil, 2017) due to uncertainties in the speed at which melts segregated, the rate of which is a function of the grain size distribution of the solid (Lichtenberg et al., 2019) and the density difference between the melts

and solid residue (Fu & Elkins-Tanton, 2014). Here, we instead treat the magma ocean as crystal slurry with a highly temperature-dependent viscosity that convects if its Rayleigh number is high enough. The presence of a convecting magma ocean increases the rate of core cooling, which has been shown in previous studies to drive thermal convection in the core that is vigorous enough to generate a dynamo field (Bryson et al., 2019b). In this work, we build on this earlier model by explicitly considering stratification at the top of the core immediately following core formation and include the effects of gradual accretion and core formation on the thermal state of the core, with implications for thermal dynamo generation.

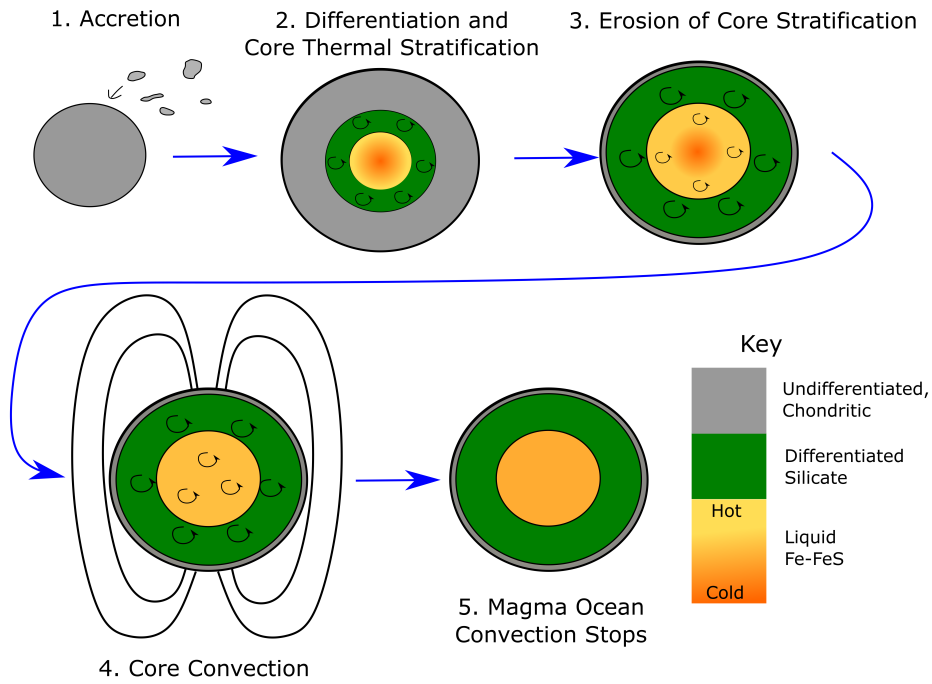


Figure 2. Schematic of planetesimal thermal evolution Grey, green and orange regions represent undifferentiated chondritic, silicate mantle and core material respectively. Shading in a given region (e.g. orange (cold) to yellow (hot) in the core during Stage 2) represents thermal stratification across the region. Diffusive heating of the core during the first 4 Myr of the planetesimal’s history could lead to a stably stratified core that inhibits core convection and dynamo generation. This stratification must be eroded (Stage 3) before the core can convect and potentially generate a dynamo field (Stage 4). Finally, the thermal forcing wanes and magma ocean convection stop (Stage 5).

2.2 Model Description

We begin our calculations of planetesimal evolution with an initial seed radius R_0 at time t_0 , composed of cold, porous chondritic material that has ^{26}Al distributed homogeneously throughout. The material has an initial temperature, $T_0 = 200$ K and it has an initial porosity $\phi_0 = 0.25$, similar to the porosity of surface lunar rocks (Warren, 2001). This porosity gives the material an initial density of

$$\rho_0 = \rho_b(1 - \phi_0) \quad (1)$$

where ρ_b is the bulk density of the body (both silicate and metal portions). For a planetesimal that contains sufficient metal to form a core that is half the body radius, we set $\rho_b = 3500 \text{ kg m}^{-3}$, which results in $\rho_0 = 2625 \text{ kg m}^{-3}$, given an initial porosity of 25%.

Stage 1 of the model consists of the diffusive heating of this seed planetesimal by the decay of ^{26}Al whilst the planetesimal accretes chondritic material to its surface. As the chondritic material heats up, it sinters and loses its porosity, which leads to a decrease in planetary radius as well as an increase in the thermal conductivity of the body. The power available from the decay of ^{26}Al to heat up the planetesimal depends on the time at which the material is accreted to the body. ^{26}Al has a half-life of $t_{1/2} = 0.717$ Myr (Neumann et al., 2014) and is therefore effectively exhausted after 3–4 Myr after CAI formation. The heating power per unit mass from the decay of ^{26}Al decay as a function of time is given by

$$H = H_0 Al_0 X_{Al} e^{-\frac{t}{t_{1/2}}}, \quad (2)$$

where H_0 is the heating power per unit mass of ^{26}Al at $t = 0$ Myr, $Al_0 = 5 \times 10^{-5}$ is the ratio of ^{26}Al to ^{27}Al in the accreting material at $t = 0$ Myr for which we take the canonical value (Elkins-Tanton et al., 2011) and $X_{Al} = 1.4 \text{ wt\%}$, the weight percentage of aluminium in the accreting material (Doyle et al., 2015).

The planetesimal grows from its initial to final radius, R_p , over a time interval, Δt_{ac} . We have adopted a general exponential form for the accretion law (Neumann et al., 2012) so that the radius of the protoplanetary body is given by

$$R_{\phi_0}(t) = R_{0,\phi_0} \left(\frac{R_{p,\phi_0}}{R_{0,\phi_0}} \right)^{\frac{(t-t_0)}{\Delta t_{ac}}} \quad (3)$$

where the R_{ϕ_0} is the uncompacted, high porosity radius, $R_{0,\phi_0} = R_{\phi_0}(t = t_0)$ is the initial uncompacted seed radius and R_{p,ϕ_0} is the final uncompacted radius at time $t = t_0 + \Delta t_{ac}$.

The newly accreted material is added to the surface of the planetesimal with the same initial temperature and porosity as the material that originally made up the starting seed planetesimal. We do not consider heating by impacts as this is a localised and stochastic heat source or heating by release of gravitational energy as the magnitude of this is negligible compared to the heating provided by the decay of ^{26}Al for small planetary bodies. ^{26}Al is distributed homogeneously within the added material with a heating power given by equation 2 evaluated at the time the material was added.

As the ^{26}Al decays, it heats up the planetesimal. Some of this heat is lost from the surface of the planetesimal (see below and Supporting Figure 1). Initially, heat loss occurs by conduction whilst the chondritic material is still cold and highly viscous. The conductive temperature profile throughout the body is modelled by a 1-D radial diffusive heat transfer equation that accounts for the internal heating provided by ^{26}Al

$$\rho c_p \frac{\partial T}{\partial t} = \frac{1}{r^2} \frac{\partial}{\partial r} \left[k r^2 \frac{\partial T}{\partial r} \right] + H \quad (4)$$

where ρ is the density of the material, c_p is the specific heat capacity of the material and k is the thermal conductivity of the material. Both the density and thermal conductivity of the material are functions of its porosity, which sinters and loses its porosity at ~ 700 K (Yomogida & Matsui, 1984). Further description of this sintering process and associated porosity evolution is detailed below.

In general, the surface temperature of the planetesimal will be given by matching the heat flux to the surface from the interior with the radiative flux from the Sun and the radiative heat flux from the surface to space. However, for the range of surface heat

fluxes produced by the cooling of the body's interior ($0.1\text{--}20\text{ W m}^{-2}$), the equilibrium surface temperature for a planetesimal situated in the asteroid belt will vary by $< 10\text{ K}$ throughout its evolution (Supporting Figure 1). Therefore, we instead impose a constant surface temperature, $T_s = 200\text{ K}$, when solving equation 4. This is the same approach adopted by Henke et al. (2013) and Bryson et al. (2019b). Due to spherical geometry, we additionally impose regularity of the thermal profile at the planetesimal centre,

$$\frac{\partial T(0, t)}{\partial r} = 0. \quad (5)$$

As the chondritic material heats up, it sinters and loses its porosity. This leads to an increase in both the density of the material and its thermal conductivity (Krause et al., 2011, Warren, 2011). The porosity evolution with temperature is given by (Yomogida & Matsui, 1984, Neumann et al., 2014)

$$\frac{\partial[\ln(1 - \phi)]}{\partial t} = A_\phi \sigma_g^{\frac{2}{3}} b^{-3} \exp\left(\frac{-E_\phi}{R_g T}\right) \quad (6)$$

where $A_\phi = 3.8 \times 10^{-5}\text{ N}^{-\frac{2}{3}}\text{ m}^{\frac{5}{3}}$ is an experimentally-determined pre-factor (Schwann & Goetze, 1978), σ_g is the stress acting on the grain boundaries, b is the size of the grains (which we take to be 1 mm), E_ϕ is the activation energy for the sintering process, R_g is the gas constant and T is the temperature of the grain. The stress acting on the grain boundary is a function of the hydrostatic pressure the grain is under. The hydrostatic pressure is given by

$$\frac{\partial P}{\partial r} = -\rho(r)g(r), \quad (7)$$

subject to the surface condition

$$P(R(t), t) = 0, \quad (8)$$

where $R(t)$ is the planetesimal radius at that time and the gravitational acceleration is given by

$$g(r) = \frac{G}{r^2} \int_0^r s^2 \rho(s) ds \quad (9)$$

where the density structure $\rho(s)$ is calculated from the porosity structure of the body.

Following Kakar and Chaklader (1967) and Rao and Chaklader (1972), the grain boundary stress is given by

$$\sigma_g = \frac{\pi P}{2\sqrt{3} \left[-1 + [4\sqrt{3}(1 - \phi)^{\frac{2}{3}} f^2(\phi)] \right]}, \quad (10)$$

where $f(\phi)$

$$f(\phi) = \frac{1}{2} \left(\frac{3}{\pi(2\sqrt{g(\phi)}(3 - g(\phi)) - 3)} \right)^{\frac{1}{3}} \quad \text{and} \quad g(\phi) = \left(\frac{1 - \phi_0}{1 - \phi} \right)^{\frac{2}{3}}. \quad (11)$$

The Arrhenius term on the right-hand side of equation 6 leads to a rapid loss of porosity from 25% to 0% at 700 K and an increase in thermal conductivity by a factor of 10 (Warren, 2011). Warren (2011) gives an expression for the thermal conductivity

$$k(\phi) = k_m \exp(-12.46\phi), \quad (12)$$

where k_m is the thermal conductivity of the compacted material. The thermal conductivity of the planetesimal depends on the type of chondritic material from which it is made. Opeil et al. (2010) measured a range in meteorite thermal conductivities from 0.5–5 W m⁻¹ K⁻¹. In this work, we use three different thermal diffusivities $\kappa = \frac{k}{\rho c_p} = 6, 9, 12 \times 10^{-7}$ m² s⁻¹ to cover this range and enable better comparison of the model results to the paleomagnetic record. These are the same thermal diffusivities used by Bryson et al. (2019b).

After sintering and compaction at 700 K, the body continues to heat up due to the decay of ²⁶Al. The onset of Fe-FeS metal melting occurs at the eutectic temperature, $T_{\text{eu}} = 1234$ K (Scheinberg et al., 2016). Depending on the sulfur content of the metal, complete metal melting will occur over the temperature interval of 1234–1810 K. For simplicity, we assume that the metal in our model is at the Fe-FeS eutectic composition of 32 wt% S so that metal melting occurs entirely at 1234 K. When a node reaches the metal melting temperature, the temperature of the node is held constant until all the metal is melted. The change in metal melt fraction, χ_{Fe} , is given by

$$\begin{aligned}
\rho_{Fe} L_{Fe} \frac{\partial \chi_{Fe}}{\partial t} &= 0, \quad T < 1234 \text{ K}, \quad \chi_{Fe} = 0 \text{ wt\%} \\
\rho_{Fe} L_{Fe} \frac{\partial \chi_{Fe}}{\partial t} &= \frac{1}{r^2} \frac{\partial}{\partial r} \left(k r^2 \frac{\partial T}{\partial r} \right) + H, \quad T = 1234 \text{ K}, \quad 0 \text{ wt\%} < \chi_{Fe} \leq 28 \text{ wt\%} \\
\rho_{Fe} L_{Fe} \frac{\partial \chi_{Fe}}{\partial t} &= 0, \quad T > 1234 \text{ K}, \quad \chi_{Fe} = 28 \text{ wt\%},
\end{aligned} \tag{13}$$

where ρ_{Fe} and L_{Fe} are the density and latent heat respectively of eutectic Fe-FeS metal solid. Once the metal is fully melted, the body continues to heat up following equation 4.

This metal melt is denser than the surrounding solid silicates and could percolate through the solid silicate matrix to the centre of the body to form a core. However, whether a core can form in a small planetary body by percolation of metal melt through a solid silicate matrix is uncertain. This is due to the high dihedral angle between the metal melt and silicate grains ($> 120^\circ$, Shannon & Agee, 1996) which requires a high metal melt fraction ($> 10\%$, Laporte & Provost, 2000) to be present before percolation will start in the body. However, experiments by Holzheid et al. (2000) show that the dihedral angle of an eutectic Fe-FeS melt is $94\text{--}106^\circ$ which decreases the percolation threshold to $3\text{--}7\%$ vol metal melt (Laporte & Provost, 2000) and promotes core formation by percolation (Néri et al., 2019).

The low gravity of these planetesimals and high viscosity ($> 10^{20}$ Pas) of the solid silicate matrix could lead to very low percolation velocities and long ($> \text{Myr}$) core formation timescales, depending on permeability of the matrix (Supporting Figure 2). These long core formation timescales, calculated using the measured permeability of chondritic meteorites from Corrigan et al. (1997), contrast with the measured Hf-W ages of magmatic iron meteorites which imply differentiation and core formation in their parent bodies was rapid and occurred by $0.6\text{--}2 \text{ Myr}$ after CAI formation (Kruijer et al., 2012, Kruijer et al., 2014).

If the melt fraction of the silicates reaches $> 50\%$, the rheological transition from solid-like to liquid-like viscosities dramatically decreases the core formation timescales to match those determined from Hf-W dating. However, whether such high melt fractions were present in meteorite parent bodies is uncertain (Wilson & Keil, 2017) and it is more likely that the presence of $> 20\%$ silicate melt fraction in the body will promote the onset of solid-state convection which provides shear stresses that create melt path-

ways along which the Fe-FeS can easily flow to the centre to form a core. Given that ^{26}Al quickly heats the interior of the body up to supersolidus temperatures on 100 kyr timescales (Supporting Figure 2), it is likely that the main epoch of core formation occurs during solid-state convection of the body with only a minor component of Fe-FeS melt percolating to the centre of the body prior to this. Thus, in our model, we consider the onset of differentiation and core formation (Stage 2) as the onset of convection, which requires $> 20\%$ silicate melting.

The silicate portion starts to melt at 1400 K and the melt fraction increases linearly across the interval 1400 – 1800 K. As such, the silicate melt fraction is

$$\chi_{sil} = \frac{T - T_{sil,s}}{T_{sil,l} - T_{sil,s}} \quad (14)$$

where $T_{sil,l}$ and $T_{sil,s}$ are the silicate liquidus and solidus temperatures, respectively.

We take into account the latent heat required for this melting by using an effective specific heat capacity (Merk et al., 2002),

$$c_{p,eff} = c_{p,m} \left[1 + \frac{L_{sil}}{c_{p,m}(T_{sil,l} - T_{sil,s})} \right], \quad 1400K < T < 1800K \quad (15)$$

where L_{sil} is the silicate latent heat. Given the values in Table 1, the modified heat capacity is approximately 2 $c_{p,m}$.

Both the increase in temperature and melt fraction leads to a decrease in the viscosity of the silicate material. Below $T < 1600$ K or $\chi_{sil} < 50\%$ silicate melt fraction, the silicates have a relative high viscosity $> 10^{14}$ Pas. There is a rapid decrease in viscosity from 1600–1650 K around the critical melt fraction of $\chi_{sil} \simeq 50\%$ as the silicates transition from a solid-like rheology to a liquid-like rheology with a viscosity $< 10^2$ Pas. This temperature-dependent viscosity is a modified version of the viscosity profile adopted by Sterenborg and Crowley (2013) and Bryson et al. (2019b) and has a similar form to the observed dependence on crystal fraction as described by Costa (2005).

We adopt a temperature-dependent silicate viscosity of the form

$$\log_{10}[\eta(T)] = 64 - \frac{T}{29} - 5 \tanh\left(\frac{T - 1625}{15}\right) \quad (16)$$

where the constants have been fitted to the profile used in Sterenborg and Crowley (2013) and Bryson et al. (2019b) as shown in figure 3.

Convection first starts over that portion of the planetesimal where the local Rayleigh number exceeds the critical value required. This leads to the start of Stage 2 and core formation below a semi-molten magma ocean. The planetesimal does not need to be fully accreted by this point. The local Rayleigh number, $Ra(r)$, is defined between a given radius and the centre of the body as this is the distance over which the convection may occur. The local Rayleigh number given by

$$Ra(r) = \frac{\rho \alpha_{sil} g r^3 (T(r) - T_b)}{\kappa \eta}, \quad (17)$$

where all the terms are evaluated at the given radius, α_{sil} is the thermal expansivity of the silicates and T_b is the temperature of the central node of the body. The critical Rayleigh number required for a given radius to start convecting is given by (Appendix B in Robuchon and Nimmo (2011))

$$Ra_{crit}(r) = 20.9 \left[\frac{E_\eta}{R_{gas} T_{ref}^2} (T(r) - T_{ref}) \right]^4, \quad (18)$$

where E_η is the activation energy for vacancy movements required for diffusion creep (300 kJ mol⁻¹, Sterenborg and Crowley (2013)) and T_{ref} is the viscosity reference temperature of 1800 K.

There are two endmembers predicted by this model of accretion and differentiation. If the planetesimal accretes rapidly over a timescale on the order of 10⁴–10⁵ years, it heats up quickly with a small temperature difference within the body (with the exception of the top 1-2km which are cold due to radiant heat loss to space). Therefore, since the Rayleigh number is proportional to r^4 (as $Ra \propto r^3 g$ where $g \propto r$), the peak in Rayleigh number occurs at radii near the surface. This leads to convection starting over most of the planetary radius. After the onset of convection, the liquid metal is rapidly segregated to the centre of the body to form a core and the semi-molten silicates form a convecting magma ocean that loses heat to space. Core formation in this case is short-lived (a few 100 kyr) with the core forming at close to its final size of half the planetary radius. If the planetesimal instead accretes more gradually over a duration of 10⁵–10⁶ years, there is a large temperature difference between the interior of the body and shallower depths. This leads to very high (> 10²⁰ Pa s) viscosities in outer layers of the body.

This high viscosity lowers the Rayleigh number at higher radii. Therefore, the radius with maximum Rayleigh number, which becomes supercritical first, is at an intermediate radius and the body initially starts convecting over only a portion of the interior. A small core forms from the liquid metal in this portion that then grows as the undifferentiated material above the magma ocean continues to heat up and subsequently differentiate. In this case, complete core formation can take on the order of a million years.

After the body starts convecting over some interior portion, the liquid metal is instantly segregated to form a core. The metal-depleted silicate portion forms a convecting magma ocean of depth d at a well-mixed magma ocean temperature T_m given by the average temperature of the differentiated portion. The core's initial temperature T_c is equal to the magma ocean temperature at differentiation. Due to the lithophilic nature of aluminium, we assume that the ^{26}Al segregates entirely into the semi-molten silicate magma ocean. Technically, the ^{26}Al will partition into the silicate melt fraction as aluminium is an incompatible element. However, we assume that the silicate melt and solid phases are always in good thermal contact and treat ^{26}Al as well mixed throughout the magma ocean. Thus the partitioning of ^{26}Al into the magma ocean removes the heat source from the core. We note that including the short-lived radioisotope ^{60}Fe as a heat source for the core only leads to 20 K temperature increase in the core over 10 Myr and the heat from the release of gravitational potential energy on core formation is also negligible (Henke et al., 2013).

The magma ocean and any overlying undifferentiated chondritic outer layers will continue to heat up as the ^{26}Al decays further. The magma ocean loses heat both to the surface and to the core as the base of the magma ocean becomes hotter than the top of the core, as shown schematically in Figure 4. The heat flux lost to the surface by convection in the slurry-like magma ocean is given by

$$f_s = -k_m \frac{(T_s - T_m)}{\delta_u}, \quad (19)$$

where k_m is the thermal conductivity of the magma ocean. The boundary layer thickness at the top of the magma ocean δ_u is given by (Solomatov, 1995)

$$\delta_u = d \left[\frac{\gamma(T_m - T_s)}{c_1} \right]^{\frac{4}{3}} \left(\frac{Ra_m}{Ra_{m,c}} \right)^{\frac{1}{3}}, \quad (20)$$

where $c_1 = 8$, Ra_m is the Rayleigh number of the magma ocean as given by equation 17 and $Ra_{m,c}$ is the critical Rayleigh number for the cessation of convection in the magma ocean. A value of $Ra_{m,cr} = 1000$ was used here (Stereborg & Crowley, 2013). The thickness of the boundary layer at the bottom of the magma ocean is given by (Solomatov, 1995)

$$\delta_l = d \left[\frac{\gamma(T_{cmb} - T_m)}{c_1} \right]^{\frac{4}{3}} \left(\frac{Ra_m}{Ra_{m,c}} \right)^{\frac{1}{3}}. \quad (21)$$

Heat is passed across the upper boundary layer into an undifferentiated chondritic lid by diffusion. We solve the 1-D heat diffusion equation, taking into account any silicate or Fe-FeS melting, for the thermal structure in the boundary layer and chondritic crust. The bottom boundary condition in this case is

$$T(R_m, t) = T_m, \quad (22)$$

where R_m is the radius of the top of the magma ocean.

When the magma ocean is hotter than the top of the core, heat passes into the top of the core by diffusion across the core-mantle boundary (CMB). The heat flux from the magma ocean to the CMB is given by:

$$f_1 = -k_m \frac{\partial T}{\partial r} \Big|_{r=R_{cmb}^+}. \quad (23)$$

The heat flux from the CMB into the top node of the core is similarly given by

$$f_2 = -k_c \frac{\partial T}{\partial r} \Big|_{r=R_{cmb}^-}. \quad (24)$$

The temperature of the CMB, T_{cmb} , is calculated at all times by assuming flux continuity across the CMB. The thermal evolution of the magma ocean is thus given by

$$\rho_m c_{p,m} V_m \frac{\partial T_m}{\partial t} = -f_s A_s + f_1 A_{cmb} + h_m \rho_m V_m \quad (25)$$

and is driven by the power lost to the surface across the top surface of the magma ocean, A_s , the power passed into the core across the area of the CMB, A_{cmb} , and the radiogenic

power production from the decay of ^{26}Al in the volume of the magma ocean, V_m , respectively. We find that immediately after formation of the magma ocean, the magma ocean heats up rapidly. The core is subsequently heated diffusively from above by the radiogenic magma ocean. A hot layer of liquid iron develops at the top of the core and the core's thermal structure becomes stably stratified. While the CMB heat flux is directed into the core resulting in a thermal stratification, we calculate the temperature profile of the core by solving the 1-D heat diffusion equation (equation 4) subject to the flux continuity condition at the CMB.

Further differentiation of any chondritic crust at the surface of the body can occur if there is still sufficient ^{26}Al present. We apply the same Rayleigh number-based approach to this lid as we did for the entire body. As layers of the lid reach super-critical Rayleigh numbers, the silicate portion from these layers is added to the magma ocean and the liquid metal added to the top of the core. We assume the addition of both silicates to the magma ocean and metal to the core is instantaneous. We also assume the silicates mix in instantly and adjust the temperature of the magma ocean to a new well-mixed average temperature.

As the liquid metal passes through the magma ocean, we assume it thermally equilibrates and is added to the top of the core at the temperature of the magma ocean. If the magma ocean is hotter than the core, this newly added material will sit at the top of the core. If cold material is added to the top of the core, it will sink and mix with the warmer core material as it falls. This will act to mix and destroy any pre-existing stratification. We model this by mixing the added cold material into the core to the depth of neutral buoyancy of the mixture. Core formation and differentiation (Stage 2) end when the temperature of the upper boundary of the magma ocean begins to decrease as this indicates that no further material is prone to convection and differentiation.

By 3 – 4 Myr after CAI formation, all the ^{26}Al has effectively decayed and the planetesimal no longer contains any appreciable heat sources. The magma ocean and any remaining chondritic lid will start to cool. Initially, if the magma ocean is hotter than the top of the core, the magma ocean will continue to pass heat into the top of the core as well as losing it to space. However, once the magma ocean and CMB becomes colder than the top of the core, the core will also start to cool. The core can lose this heat either diffusively, if the core's thermal structure remains stably stratified or the magma

ocean cooling leads to a sub-adiabatic heat flux out of the CMB ($< 0.01 \text{ W m}^{-2}$), or by convection once portions of the core are no longer stably stratified (Stage 3, erosion of core stratification). The stably stratified region of the core is defined as the region in which $\frac{\partial T}{\partial r} > 0$. While the core is stably stratified (which occurs at early times for bodies which accrete over timescales of less than $\sim 1 \text{ Myr}$), the heat fluxes in and out of the CMB are given by equations 23 and 24 and the core temperature profile is calculated using equation 4.

After sufficient magma ocean cooling, the top of the core will become colder than the interior of the core and convection may proceed in the core. This marks the start of Stage 3, in which any thermal stratification in the core is eroded. The top of the core is mixed down to a level of neutral buoyancy (see Figure 4). This results in a well-mixed isothermal profile from the CMB to the depth of neutral buoyancy. At first, this mixed region only reaches into the top few kilometres of the core. The radius of the bottom of the well-mixed region is given by R_{con} and its thickness by d_{con} . This well-mixed region can now convect when the core cools further whilst the colder, stratified interior passes heat diffusively. The heat flux from the convecting portion of the core to the CMB is given by

$$f_2 = -k_c \frac{(T_{cmb} - T_c)}{\delta_c}, \quad (26)$$

where T_c is now the temperature of the well-mixed convecting portion of the core and $\delta_c = \left(\frac{\kappa_c \eta_c}{\rho_c \alpha_c g_c (T_c - T_{cmb})} \right)^{\frac{1}{3}}$ is the boundary layer thickness at the top of the core. The subsequent temperature change of the core's convecting region with volume V_{con} is given by

$$\rho_c c_{p,c} V_{con} \frac{\partial T_c}{\partial t} = -f_2 A_{cmb} + f_3 4\pi R_{con}^2, \quad (27)$$

where

$$f_3 = -k_c \frac{\partial T}{\partial r} \Big|_{r=R_{con}} \quad (28)$$

is the heat flux from the base of the convecting region to the top of the stratified layer. Further core cooling erodes the stable stratification and the convecting region extends into the deep interior of the core. The stratification in the core is completely removed (Stage 4) approximately at the time that the magma ocean temperature cools to

the temperature at which differentiation first occurred. This corresponds to the time at which all the heat added in the first 3 – 4 Myr to the core is removed.

We continue to calculate the temperature evolution of the convecting magma ocean using equation 25. However, the flux from the CMB to the base of the magma ocean now occurs over the lower boundary layer so that

$$f_1 = -k_m \frac{(T_m - T_{cmb})}{\delta_l}. \quad (29)$$

As the magma ocean cools, both its top and bottom boundary layers grow and the convecting depth decreases. This, along with the increase in viscosity, lowers the magma ocean’s Rayleigh number. Once the Rayleigh number of the magma ocean becomes subcritical ($Ra_m < 1000$), convection shuts off in the silicate portion of the planetesimal and heat is lost throughout the entire mantle by diffusion. This leads to a large drop in the CMB heat flux and core cooling becomes subadiabatic and convection ceases (Bryson et al., 2019b). Therefore our model ends when the magma ocean stops convecting (Stage 5) as we do not consider planetesimals to be able to generate a dynamo driven by thermal convection alone once the mantle is cooling conductively.

Finally, we quantify whether the planetesimal was able to generate a thermal dynamo during this early period of magma ocean convection by calculate the magnetic Reynolds number of the core at each time step. The magnetic Reynolds number $Re_m = ul/\lambda$ is a dimensionless measure of the strength of the convective forcing to that of the Ohmic dissipation in a dynamo where u is a characteristic convection velocity, l is the length scale of the convection and $\lambda = 1.3 \text{ m}^2 \text{ s}^{-1}$ is the magnetic diffusivity of liquid iron. In this case, we take the length scale of the convection as the depth of the convecting portion of the core. The velocity of the convective motions in the planetesimal’s core can be estimated using a balance of the magnetic, Archimedean and Coriolis (MAC) forces (Weiss et al., 2010),

$$u = \left(\frac{2\pi G \alpha_c R_c F_{drive}}{c_{p,c} \Omega} \right)^{\frac{2}{5}}. \quad (30)$$

Here Ω is the angular rotational frequency of the planetesimal for which we adopt a value of $\Omega = 1.7 \times 10^{-4} \text{ s}^{-1}$ (a period of 10 hours) to enable direct comparison of our results

with Bryson et al. (2019b), and $F_{drive} = f_2 - f_{ad}$, the superadiabatic heat flux out of the core. The core adiabatic heat flux is

$$f_{ad} = \frac{k_c \alpha_c g_c T_c}{c_{p,c}}. \quad (31)$$

There are multiple velocity scalings used in Weiss et al. (2010) and the MAC scaling we have adopted here gives velocity estimates of 10-100 times lower than the other possibilities and is therefore a conservative estimate. For dynamo generation, the critical value of Re_m is between 10 and 100 (Weiss et al., 2010). We adopt to the lower value of 10 in line with Sterenborg and Crowley (2013) and Bryson et al. (2019b). Throughout each model run, we record any time periods during which the magnetic Reynolds number is super critical and therefore the times when thermally driven dynamo activity is possible. We also record the maximum achieved Re_m and the core cooling rate at these times.

In order to solve this set of equations, we use a forward-in-time centred-in-space (FTCS) scheme with a time step of 300 yrs and initial high-porosity radial node spacing of 700m. To account for compaction and loss of porosity as the chondritic material heats up, the radial node spacing decreases as a function of node porosity. We have implemented the code on a highly resolved grid of time steps of 30 yr and verified that the model results are independent of the choice of node spacing.

Parameter	Symbol	Value	Units	Reference
Initial Temperature of Accreting Material	T_0	200	K	(Henke et al., 2013)
Initial Porosity of Accreting Material	ϕ_0	0.25		(Warren, 2001)
Half-life of ^{26}Al	$t_{1/2}$	0.717	Myr	(Neumann et al., 2014)
Heating power of ^{26}Al at $t = 0$	H_0	0.355	W kg^{-1}	(Elkins-Tanton et al., 2011)
^{26}Al / ^{27}Al Ratio at $t = 0$	Al_0	5×10^{-5}		(Elkins-Tanton et al., 2011)
Weight percentage of Al in Accreting Material	X_{Al}	1.4	wt%	(Doyle et al., 2015)
Final Radius of Planetesimal	R_p		km	
Initial Radius of Planetesimal	R_0		km	
Start Time of Accretion	t_0		Myr	
Accretion Duration	Δt_{ac}		Myr	
High-Porosity Radial Node Space	Δr_{ϕ_0}	700	m	
Radial Node Space Post-Compacting	Δr	636	m	
Time Step	Δt	300	yr	
Porosity Prefactor	A_ϕ	3.8×10^{-5}	$N^{-\frac{2}{3}} m^{\frac{5}{3}}$	(Schwann & Goetze, 1978)
Grain size of Accreting Material	b	1	mm	
Activation Energy of Sintering Process	E_ϕ	2.51	MJ mol^{-1}	(Neumann et al., 2012)
Fe-FeS Eutectic Temperature	T_{eu}	1234	K	(Stereberg & Crowley, 2013)
Density of Solid Metal	ρ_{Fe}	7800	kg m^{-3}	(Bryson et al., 2015)

Latent Heat of Fusion of Metal	L_{Fe}	270	kJ kg^{-1}	(Bryson et al., 2015)
Silicate Solidus Temperature	$T_{sil,s}$	1400	K	(Sternborg & Crowley, 2013)
Silicate Liquidus Temperature	$T_{sil,l}$	1800	K	(Sternborg & Crowley, 2013)
Latent Heat of Fusion of Silicates	L_{sil}	400	kJ mol^{-1}	(Elkins-Tanton et al., 2011)
Mantle Specific Heat Capacity	$c_{p,m}$	850	$\text{J kg}^{-1} \text{K}^{-1}$	(Elkins-Tanton et al., 2011)
Silicate Thermal Diffusivity	κ	$6, 9, 12 \times 10^{-7}$	$\text{m}^2 \text{s}^{-1}$	(Opeil et al., 2010)
Specific Heat Capacity of Core	$c_{p,c}$	850	$\text{J K}^{-1} \text{kg}^{-1}$	(Elkins-Tanton et al., 2011)
Thermal Conductivity of Core	k_c	30	$\text{W m}^{-1} \text{K}^{-1}$	(Opeil SJ et al., 2012)
Thermal Expansivity of Silicates	α_{sil}	4×10^{-5}	K^{-1}	(Sternborg & Crowley, 2013)
Viscosity Activation Energy	E_η	300	kJ mol^{-1}	(Sternborg & Crowley, 2013)
Viscosity Reference Temperature	T_{ref}	1800	K	(Robuchon & Nimmo, 2011) (maybe?)
Critical Mantle Rayleigh Number	$Ra_{m,c}$	1000		(Sternborg & Crowley, 2013)
Density of Core Liquid	ρ_c	6980	kg m^{-3}	(Morard et al., 2018)
Thermal Expansivity of Core Liquid	α_c	9.2×10^{-5}	K^{-1}	(Nimmo, 2009)
Viscosity of Core Liquid	η_c	0.01	Pa s	(de Wijs et al., 1998)
Rotational Period	t_{spin}	10	hr	(Bryson et al., 2019b)

Table 1: Parameters and values used in model

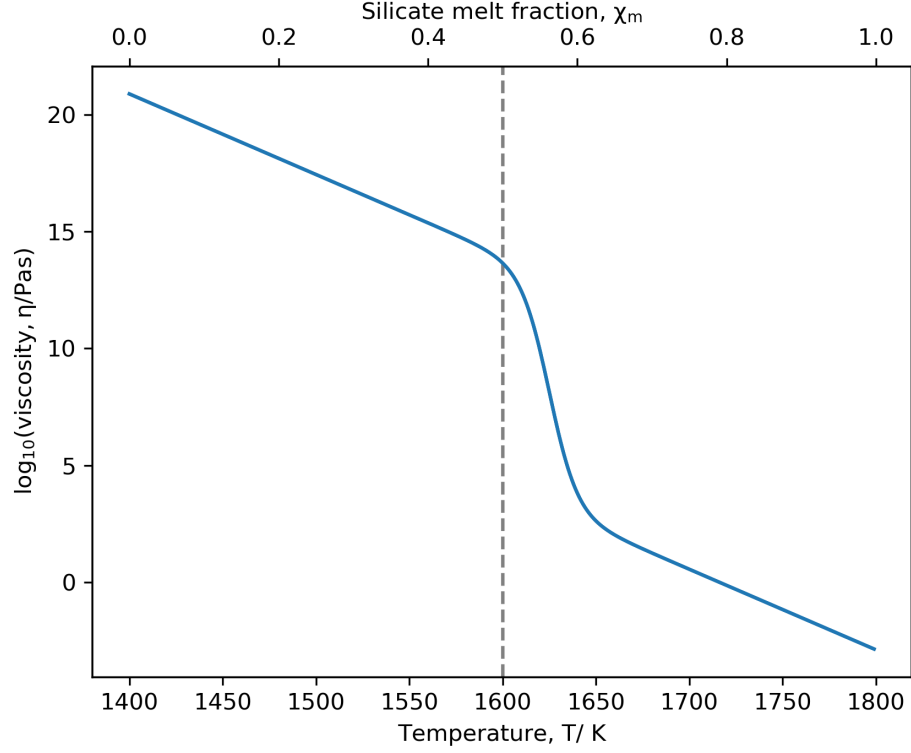


Figure 3. Modelled temperature dependence of the silicate viscosity fitted to the step functions used by Sterenborg and Crowley (2013) and Bryson et al. (2019b). We treat the silicate melt and solid as a single phase that undergoes a rheological transition from solid-like behaviour to liquid-like behaviour at the critical melt fraction of 50% (as marked by the dashed grey line). This rapid drop in viscosity around the critical melt fraction leads to an increase in Rayleigh number and promotes the onset of convection in the planetesimal.

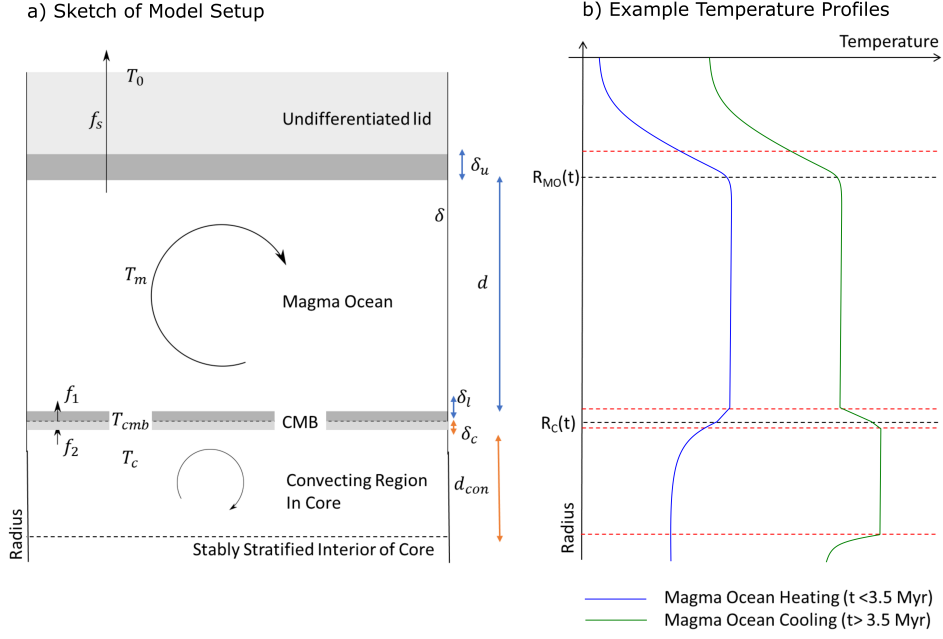


Figure 4. a) Sketch of 1D model set up and b) Example temperature profiles through a planetesimal during both magma ocean heating (blue line) and cooling (green line). Initially the magma ocean is hotter than the core due to partitioning of the ^{26}Al into the magma ocean. This leads to diffusive heating of the core from above and the build-up of a stably stratified layer at the top of the core. The temperature profile in the body during this period resembles that shown by the blue line in b). Once the magma ocean becomes colder than the top of the core, convection starts up in a thin layer at the top of the core whilst its interior remains stably stratified. This temperature profile is shown by the green line in b). Note that the apparent offset in surface temperature between the two profiles is not real and included for clarity only.

3 Results

3.1 Thermal Evolution of Case Studies

In this section, we present the results of the thermal evolution model for three specific cases to illustrate the effect of accretion duration and the timescale and process of core formation on a planetesimal's ability to generate a thermally driven dynamo. In these cases, the initial radius of the body is 170 km and the final radius is 500 km. Accretion starts at 0.8 Myr after CAI formation with the accretion duration varying between the three cases. Case 1 (Figure 5) grows "instantaneously" to its full size in 500 yr. Case 2 (Figure 6) takes 200 kyr to reach its full size and Case 3 (Figure 7) accretes material slowly over 1200 kyr.

Both Case 1 and 2 result in fully differentiated bodies with 250 km radius cores. However, the rapidly accreting body (Case 1) does not generate a thermal dynamo at any time whereas the more gradually accreting body (Case 2) generates one from 7–21 Myr after CAI formation. This is due to the difference in core formation durations, which leads to differences in the thermal structures of the cores created during this process. Case 1 forms a core rapidly that is then heated from above by the superheated magma ocean, resulting in a strong (70 K) stable stratification extending tens of kilometres below the CMB that hinders early core convection. Whole core convection in this case is delayed until 40 Myr after CAI formation (while the stratification is gradually removed through the passage of heat across the CMB) at which point the body is cooling too slowly to generate supercritical CMB heat fluxes. In the more gradual case, the stratification at the top of the core is less strong due to the majority of the core forming once the magma ocean had heated up to 1610 K (i.e., the inner part of the core is hotter than the instantaneous case, leading to weaker stratifications). This stratification is entirely removed by 10 Myr after CAI formation and the whole core convects readily during the period of fast magma ocean cooling. This body achieves a supercritical magnetic Reynolds number from 7 – 21 Myr after CAI formation. Case 3 accretes slowly with significant addition of chondritic material to its surface after 1.8 Myr after CAI formation. This material is depleted in ^{26}Al and therefore has to rely on heat passed upwards from the hotter interior in order to differentiate. As the body starts to cool, this heat is instead lost to space and the ^{26}Al -depleted layers do not melt. This results in a partially differentiated body with an inner liquid core and convecting magma ocean hidden below an un-

differentiated chondritic lid. In this body, the small size of the core leads to subcritical magnetic Reynolds numbers.

3.1.1 Case 1: *Instantaneous Accretion*

Figure 5a shows the thermal evolution of a planetesimal growing from an initial seed radius of 170 km to a final radius of 500 km in 500 yr as a function of radius and time. The position of the core is given by the black dashed line. The temperature of the magma ocean and the core (initially the top of the core then the convecting portion of the core) as a function of time is shown in Figure 5b and the evolution of the CMB heat flux and magnetic Reynolds number are shown in Figures 5c and d respectively.

For instantaneous accretion, the body heats up quickly due to the decay of ^{26}Al . Due to the speed with which the body accretes to its full size, the body heats up isothermally with only a thin 2 km thick cold lid at the surface, which is cooled by radiative heat loss to space. Therefore, at the onset of solid-state convection at 1.1 Myr after CAI formation, the inner 480 km of the body differentiates as the Rayleigh number first becomes supercritical close to the surface. A core of radius 240 km and an overlying convecting magma ocean of depth 240 km form at a temperature of 1505 K. The ^{26}Al partitions into the silicate magma ocean and the core is left without any internal heat source. This causes a period of heat transfer between 1.1 Myr and 3.5 Myr after CAI formation from the base of the magma ocean across the CMB into the top of the core while the magma ocean continues to heat up due to the decay of ^{26}Al as shown by the negative CMB heat flux in Figure 5c. The magma ocean reaches its peak temperature of 1620 K at 1.2 Myr after CAI formation (Figure 5b). The core grows by an additional 10 km to its final size of 250 km as some of the remaining chondritic lid differentiates later between 1.1 and 1.3 Myr after CAI formation. These later episodes of differentiation lead to the top of the core and magma ocean being the same temperature temporarily as the new core material is added to the top of the core at the magma ocean temperature. This results in the CMB heat flux going to zero temporarily as seen in Figure 5c. The CMB heat flux quickly becomes negative again after these episodes of core formation as the magma ocean heats up due to the decay of ^{26}Al . The timing of these further episodes of core formation is controlled by the diffusive timescale required to heat the undifferentiated lid sufficiently for it to start convecting. We have ensured our choice of time step does not affect this behaviour and subsequent thermal evolution. This step-like behaviour seen in

the CMB heat flux is a consequence of the 1D nature of our model where core formation occurs in discrete shells whereas in reality, it would be a more continual delamination of parcels of the undifferentiated lid into the convecting magma ocean. After 1.3 Myr after CAI formation, differentiation is complete and the position of the core-mantle boundary becomes fixed.

The magma ocean remains at a peak temperature $T_m > 1620$ K from 1.2-3 Myr after CAI formation whilst there is still sufficient decay of ^{26}Al present to balance the loss of heat from the surface (10 W m^{-2}) and to the core (0.05 W m^{-2}). During this period, the top 5 km of the core is heated passively from above to a temperature of 1620 K whilst the interior of the core remains at the cooler differentiation temperature of 1505 K. This introduces a stable thermal and density stratification to the core that inhibits core convection.

The magma ocean remains hotter than the top of the core until 9 Myr after CAI formation. During this period, the core is heated from above diffusively and this causes the core to become progressively more thermally stratified. At 9 Myr after CAI formation, the base of the magma ocean becomes colder than the top of the core and heat is now extracted from the top of the core. Initially, this heat transfer out of the core can occur by conduction as the temperature gradient in the core is positive and there is therefore no negative density contrast between the cooling top of the core and the material below to drive convection. However, this only occurs at very early times after the core starts to cool (1000-2000 yr at most). Once the top of the core becomes colder than the interior, a negative density difference at the top of the core now exists which may drive convection. This occurs at 9 Myr after CAI formation. The resultant convecting layer is initially ~ 2 km deep and at 1575 K. The onset of convection in the core greatly increases the CMB heat flux (figure 5c). Below this convecting layer however, the core is still stably stratified and heat is passed diffusively between the top of the stratified layer and the base of the convecting layer.

As the body continues to cool, the convecting layer in the core grows as more of the stable stratification is eroded. The associated increase in length scale of convection in the core leads to an increase in magnetic Reynolds' number (figure 5d). At 40 Myr after CAI formation, all the stable stratification has been removed and the core convects over its entire radius. This corresponds to the peak $\text{Re}_m \simeq 4.4$ at 40 Myr after CAI for-

625 mation. After this time, the magnetic Reynolds' number decreases as the CMB heat flux
 626 decreases. The magma ocean Rayleigh number drops below the critical value of 1000 at
 627 56 Myr after CAI formation and convection in the magma ocean shuts off.

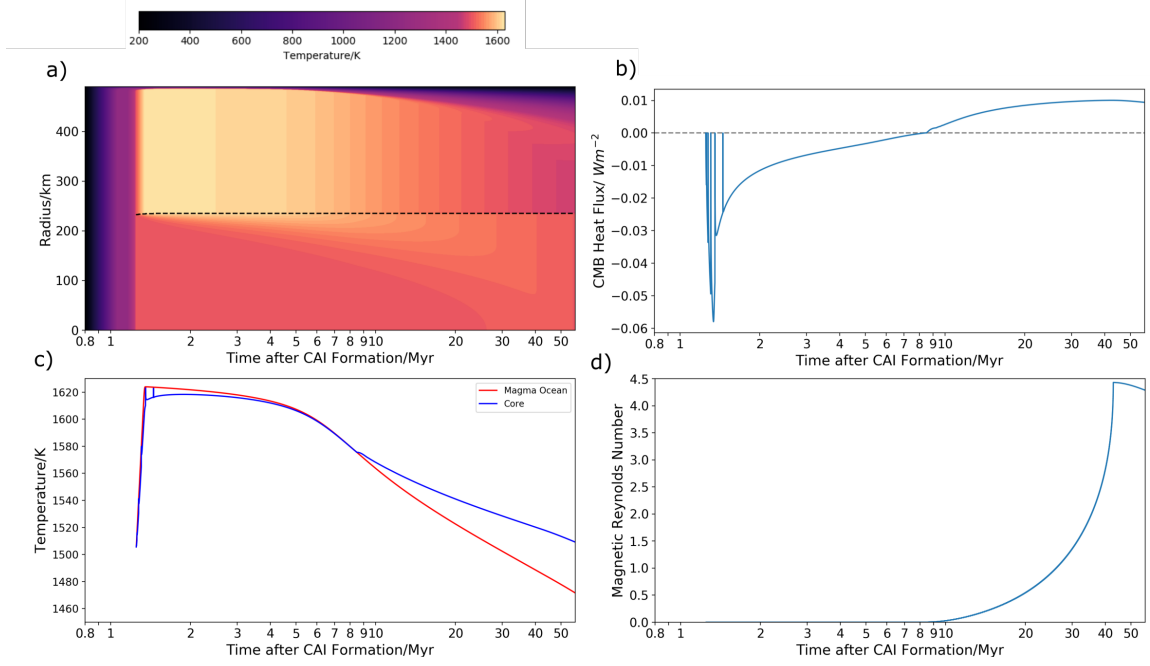


Figure 5. Case 1: a) Thermal Evolution of a Rapidly Accreting Planetesimal which grows from a 170 km seed radius to 500km over a period of 500 years. The dashed line denotes the core mantle boundary. **b) Magma Ocean and Core Temperatures.** The core temperature shown is initially that at the top of the core then the temperature of the convecting portion once the stable stratification has been removed. **c) CMB Heat Flux and d) Magnetic Reynolds Number** for this planetesimal. The top of the core becomes stably stratified during the first 4 Myr and the complete erosion of this stratification takes until 40 Myr. This inhibits whole core convection whilst the magma ocean is cooling rapidly and thus no dynamo field is generated.

3.1.2 Case 2: Intermediate Accretion Rate

Figure 6a shows the thermal evolution of a planetesimal growing from an initial seed radius of 170 km to a final radius of 500 km in 200 kyr as a function of radius and time. The position of the core is given by the black dashed line. The temperature of the magma ocean and the core (initially the top of the core then the convecting portion of the core) as a function of time is shown in Figure 6b and the evolution of the CMB heat flux and magnetic Reynolds number are shown in Figures 6c and d, respectively.

The longer duration of accretion in this case leads to a variable temperature profile with depth throughout this body as it heats up from the decay of ^{26}Al . Therefore, the onset of convection in the body first occurs over the inner 150 km of the body at a temperature of 1550 K, 1.1 Myr after CAI formation. At this time, the chondritic material at larger radii is too cool and viscous to start convecting. This effect creates a core of 75 km in radius and a 75 km deep convecting magma ocean under a thick undifferentiated lid that is still heating up. This undifferentiated lid insulates the deep magma ocean, which quickly heats up to > 1600 K at 1.2 Myr after CAI formation. Heat is passed diffusively into the top of the core and the temperature of the core is approximately isothermal with the magma ocean during this period (Figure 6b).

Simultaneously, the undifferentiated shallower regions in the body heat up due to the decay of ^{26}Al and the viscosity in these regions decreases. Between 1.4 and 1.8 Myr, convection starts across these shallower depths and these regions undergo differentiation. Subsequently the top 250 km of the body differentiates during this time period. The material from shallower depths is cooler (~ 1450 K) than the magma ocean and its addition to the far hotter magma ocean ($T_m \simeq 1620$ K at 1.4 Myr after CAI formation) results in cooling of the magma ocean to ~ 1580 K. The new core material is then incorporated into the core at this new magma ocean temperature. This material is cooler than the top (10s of km) of the core and thus sinks when it enters the core. The stratification at the top of the core is destroyed by the addition of this cool material and the core becomes well mixed over the top 180 km with a temperature $T_c \simeq 1600$ K. This leads to a brief 100 kyr interval during which the top 180 km of the core passes heat by convection into the magma ocean which is shown by the spike in CMB heat flux and magnetic Reynolds number at this time. The magma ocean is rapidly heated back up to ~ 1620 K by the decay of ^{26}Al and the CMB heat flux becomes negative as heat is passed

from the base of the magma ocean to the top of the core. A thin, stably stratified layer develops at the top of the core with a depth of < 5 km and temperature of 1615 K.

At 4 Myr after CAI formation, the supply of ^{26}Al is exhausted and the magma ocean cools below the temperature of the top of the core. Core convection over a shallow depth below the CMB starts immediately and the convective layer quickly grows. This leads to a rapid increase in the magnetic Reynolds (Figure 6d). The CMB heat flux also increases as the CMB temperature difference increases, which contributes to this increase in magnetic Reynolds number. By 7 Myr after CAI formation, the core is convecting over the top 200km and its magnetic Reynolds number exceeds the critical value of 10 such that the core is able to generate a thermally driven dynamo field. Whole convection occurs at 10 Myr after CAI formation and results in a peak magnetic Reynolds number of 14. From 10 Myr after CAI formation onwards, the magnetic Reynolds number decreases in line with the decreasing CMB heat flux. It becomes subcritical at 21 Myr after CAI formation and the dynamo field shuts off. The magma ocean convection continues until 56 Myr after CAI formation.

The increased timescale of core formation in this case compared to the instantaneously accreting planetesimal results in a core thermal structure that is easily able to convect over most of its depth once core cooling commences. This enables core convection in the first 20 Myr whilst the magma ocean is losing heat rapidly to the surface, resulting in high enough CMB heat fluxes to generate supercritical magnetic Reynolds numbers.

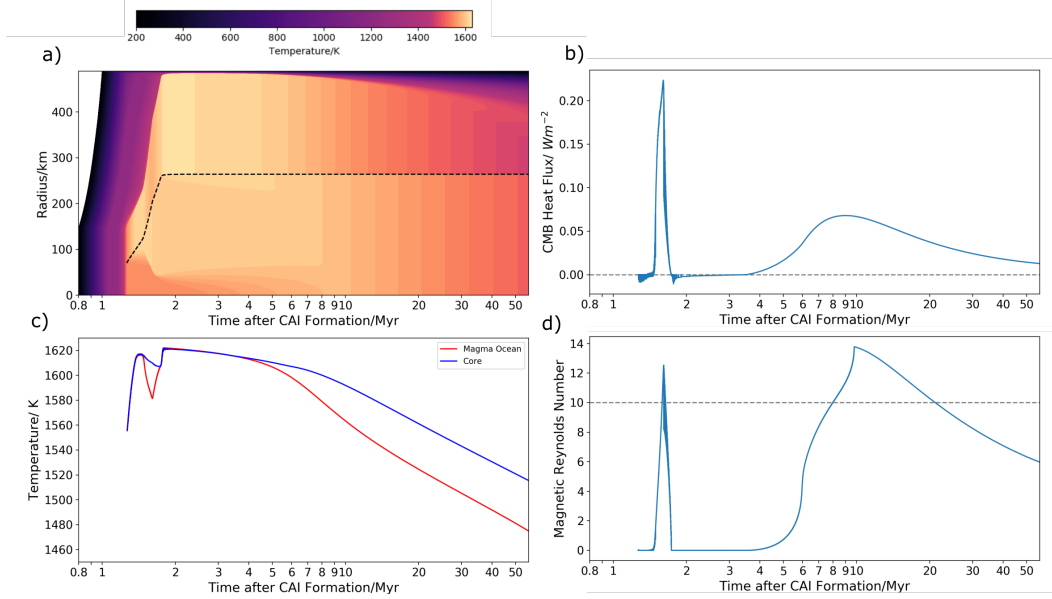


Figure 6. Case 2: a) Thermal Evolution of a Gradually Accreting Planetesimal which grows from a 170 km seed radius to 500km over a period of 100 000 years. The dashed line denotes the core mantle boundary. **b) Magma Ocean and Core Temperatures.** The core temperature shown is initially that at the top of the core then the temperature of the convecting portion once the stable stratification has been removed. **c) CMB Heat Flux and d) Magnetic Reynolds Number** for this planetesimal. The top 190 km of the core forms once the magma ocean has heated up to ~ 1600 K. Therefore once the core starts to cool at 3.5 Myr, the core is less strongly stratified underneath the CMB and convection starts over the top 190 km at 5 Myr whilst the deep-seated stratification is quickly eroded by 9.3 Myr. This difference in core formation mechanism allows for whole core convection whilst the magma ocean is cooling rapidly and the generation of a thermally driven dynamo field from 7 to 21 Myr.

3.1.3 Case 3: Slow Accretion Rate

Figure 7a shows the thermal evolution of a planetesimal growing from an initial seed radius of 170 km to a final radius of 500 km in 1.2 Myr as a function of radius and time. The position of the core is given by the black dashed line. The temperature of the magma ocean and the core (initially the top of the core then the convecting portion of the core) as a function of time is shown in Figure 7b and the evolution of the CMB heat flux and magnetic Reynolds number are shown in Figures 7c and d, respectively.

The chondritic material that accretes prior to 1.8 Myr after CAI formation contains enough ^{26}Al to drive melting and differentiation of the body. However, the material that accretes after this time only contains sufficient ^{26}Al to heat the material without causing it to melt. The onset of convection and differentiation in this body occurs at 1.2 Myr after CAI formation, before the body is fully accreted. In a similar manner to the intermediate accretion rate example (Case 2), the body first differentiates over a deep interior portion up to a radius of 150 km. This process forms a small 75 km core under a shallow 75 km deep magma ocean. The temperature of differentiation is 1560 K. At this time, the body is 200 km in total radius. The magma ocean quickly heats up to ~ 1620 K (figure 7b). Differentiation in the 50 km lid above the magma ocean as well as in the new material added to the surface after 1.2 Myr can be driven by both the decay of ^{26}Al and heating from below by the hot (1620 K) magma ocean. The steep thermal gradient across the undifferentiated lid leads to gradual differentiation of layers 1-2 km above the magma ocean. While this newly differentiated material is cooler than the magma ocean (similar to the previous case), the volume of material that is added to the magma is reduced and thus its cooling effect on the magma ocean temperature is reduced. As a consequence, the magma ocean remains hotter than the core for the first 4 Myr after CAI formation. The CMB heat flux goes to zero at each addition of new material to the core as the top of the core and the magma ocean are temporarily isothermal, giving rise to the seemingly stochastic jumps in Figure 7. Prior to 3-4 Myr after CAI formation, the CMB heat flux then quickly falls below zero again as the magma ocean becomes hotter than the top of the core due to the decay of ^{26}Al . This results in the sawtooth pattern in both the CMB heat flux (Figure 7c) and magnetic Reynolds number (Figure 7d). Again, this is a consequence of the 1D nature of our model and its inability to model core formation as a smooth, continuous process and the timescale of these jumps is set by the diffusive timescale required for the next layer to reach its critical Rayleigh

number. We have shown an effective CMB heat flux and magnetic Reynolds number on Figures 7c and d, which is the average of the respective quantity for each episode of core formation and thermal evolution between episodes, in order to give a clearer picture of the evolution of both these values.

Chondritic material that accretes to the surface of the planetesimal after 1.8 Myr after CAI formation does not contain sufficient ^{26}Al to differentiate by internal heating from this heat source alone. However, differentiation is able to continue after 1.8 Myr after CAI formation in the layers directly above the magma ocean as the magma ocean provides an additional heat source to drive melting in these layers. This is seen in Figure 7a as the core radius increases from 90 km at 1.8 Myr to 110 km at 10 Myr after CAI formation, the time at which core formation ends in this case.

The magma ocean first becomes colder than the top of the core at 1.8 Myr after CAI formation at a temperature of 1625 K, at which point the CMB heat flux becomes positive. The oscillation between high and low positive values is due to the continued addition of discrete delamination events of cool material from the cold lid to both the magma ocean and the core as differentiation proceeds. This acts to reduce the CMB temperature difference and thus the CMB heat flux. In the periods between episodes of differentiation, the magma ocean cools faster than the top of the core which increases the CMB temperature difference and thus CMB heat flux.

Core formation ends at 10 Myr after CAI formation with a core of 110 km, magma ocean depth of 110 km and with the top 280 km remaining undifferentiated. However, much of this undifferentiated lid would not be expected to preserve its chondritic texture. The bottom 50 km of the lid directly above the magma ocean has been heated to peak temperatures above the Fe-FeS eutectic liquidus, and above the silicate liquidus for the inner 30 km of this portion. This partial melting will destroy the original chondritic texture of the material at these depths. Instead, this material could be somewhat similar in petrology and texture to primitive achondrites. Convection in the magma ocean ceases shortly afterwards at 11 Myr. The magnetic Reynolds number in this case remains subcritical for the entire period of magma ocean convection, due to small size of core.

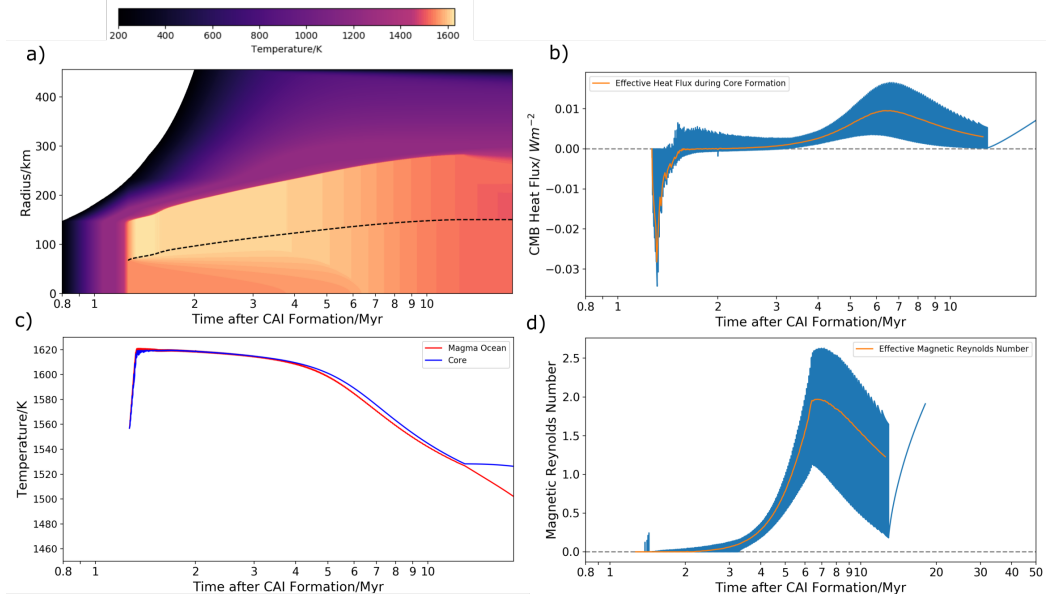


Figure 7. Case 3: a) Thermal Evolution of a Slowly Accreting Planetesimal which grows from a 170 km seed radius to 500km over a period of 1.2 Myr. The dashed line denotes the core mantle boundary. **b) Magma Ocean and Core Temperatures.** The core temperature shown is initially that at the top of the core then the temperature of the convecting portion once the stable stratification has been removed. **c) CMB Heat Flux and d) Magnetic Reynolds Number** for this planetesimal. We show both the model output per timestep of these quantities (blue lines) as well as the effective quantities (orange lines), which represents the average of these quantities during core formation. This body accretes the outer 250km of its radius after 1.8 Myr by which time these layers do not contain sufficient ²⁶Al to differentiate. This results in a partially differentiated body with a molten core and convecting magma ocean below an undifferentiated chondritic lid.

	n	t_0 / Myr	Δt_{ac} / Myr	R_0 /km	R_p /km
Sweep 1	5000	0.01-2	0.005-4	70-545	70-550
Sweep 2	5000	0.01-1.8	0.005-1.2	70-400	400-550

Table 2. Input values for two random parameter sweeps of $n = 5000$ simulations. The accretion start t_0 , duration Δt_{ac} , initial and final radii R_0 and R_p , of the planetesimal were randomly chosen using the inbuilt Random package in Python for each simulation. The radii given here are compacted lengths, that is with no porosity in the body. The values for Sweep 2 were based on the results of Sweep 1 and were chosen to target the region of parameter space in which the models exhibit dynamo generation.

3.2 Parameter Sweeps

In the previous section, the results of three example model runs were presented to show the effect of accretion rate and the duration of core formation on a planetesimal’s ability to generate a thermally-driven dynamo. In this section, we present the results of two parameter sweeps of our four input variables - accretion start time and duration, and initial and final body radius - to constrain the impact that these parameters have on the properties of thermally driven dynamo activity in meteorite parent bodies. We also show the results of the structures of planetesimals we obtain in our models.

For each of our three values of the mantle thermal diffusivity, we ran two parameter sweeps of 5000 model runs with randomly sampled combinations of accretion start time, duration, initial and final body radius. These 5000 simulations spanned the entire parameter space. We subsequently performed 5000 simulations on a subset of initial parameter, focusing on those parameter combinations known to produce thermally-driven dynamos. Table 2 gives the range of input values for both sets of simulations for all three silicate thermal diffusivities studied. The results presented here are for a silicate thermal diffusivity of $\kappa = 9 \times 10^{-7} \text{m}^2 \text{s}^{-1}$. The full results of the other two are included in the Supplementary Materials (Figures 3 and 4).

3.2.1 Controls on Dynamo Generation

Figure 8a shows the dependence of the initial and final radius of the planetesimal on its potential to create a thermally driven dynamo. A final planetary radius of > 410 km and an initial radius of < 350 km is required for bodies with a thermal diffusivity of $\kappa = 9 \times 10^{-7} \text{ m}^2 \text{ s}^{-1}$. This corresponds to a minimum core size of ~ 205 km. For a larger $\kappa = 12 \times 10^{-7} \text{ m}^2 \text{ s}^{-1}$, this requirement is $R_0 < 380$ km and $R_p > 395$ km while for a smaller $\kappa = 6 \times 10^{-7} \text{ m}^2 \text{ s}^{-1}$, this requirement is $R_0 < 340$ km and $R_p > 430$ km.

The constraint on magnetic field generation for initial radii of < 350 km comes from the requirement of gradual core formation to avoid strong stable stratification at the top of the planetesimal core. If the planetesimal grows by more than 250 km in radius over > 100 kyr, this promotes more gradual core formation and early onset of whole core convection to coincide with the period of quickest magma ocean cooling. However, there are many runs that fulfilled the initial and final radii constraints that did not produce a supercritical magnetic Reynolds at any point in their history. This is due to dependence of magnetic field generation on the start time of accretion and accretion duration which is shown in Figures 8b and 8c, respectively. In both these figures, runs that did not produce planetesimals with cores greater than 205 km in radius have been excluded.

In order to generate a thermal dynamo, the planetesimal needs to accrete in the first 1.4 Myr after CAI formation and grow by a minimum of 210 km in radius over duration of 100-1200 kyr. Bodies that accrete later than 1.4 Myr after CAI formation but with the necessary accretion duration and growth amount do not fully differentiate, therefore their cores are too small to produce a magnetic Reynolds number $Re_m > 10$. Equally, a planetesimal can accrete very early but if its accretion rate is too fast (either due to a short accretion duration or small radial increase during accretion), core formation is very quick and a strong stable stratification forms at the top of the core that inhibits core convection until after the main peak of magma ocean cooling.

The start time of thermal dynamo generation in these bodies is controlled by the initial radius of the planetesimal (Figure 8d) as this controls how fast the core forms and the strength of the thermal stratification at the top of the core. The earliest time at which we predict thermal dynamo generation is 4 Myr after CAI formation as before this time, there is still sufficient ^{26}Al to keep the magma ocean from cooling and the core is heated from above by the magma ocean. Only once all the ^{26}Al has decayed can the core start

cooling and potentially convecting. The time at which the core can then start to con-
 vect over a depth of 205 km or greater is controlled by the thickness and strength of the
 stratification at the top of the core. The earliest start times are 4 Myr and 4.5 Myr af-
 ter CAI formation for thermal diffusivities of $\kappa = 12 \times 10^{-7} \text{ m}^2 \text{ s}^{-1}$, $6 \times 10^{-7} \text{ m}^2 \text{ s}^{-1}$
 respectively. The radius of the planetesimal controls how quickly the body cools once
 the ^{26}Al has decayed and therefore when the thermal dynamo generation shuts off (Fig-
 ure 8e). In all cases, the thermal dynamo shuts off before the end of the period of con-
 vection in the magma ocean and we do not expect thermally driven dynamo activity in
 any planetesimals after 34 Myr after CAI formation.

Table 3 summarises the dependence of thermal dynamo generation in planetesimals
 on the model input parameters for the three thermal diffusivities we investigated as well
 as the range of start and end times of these dynamos.

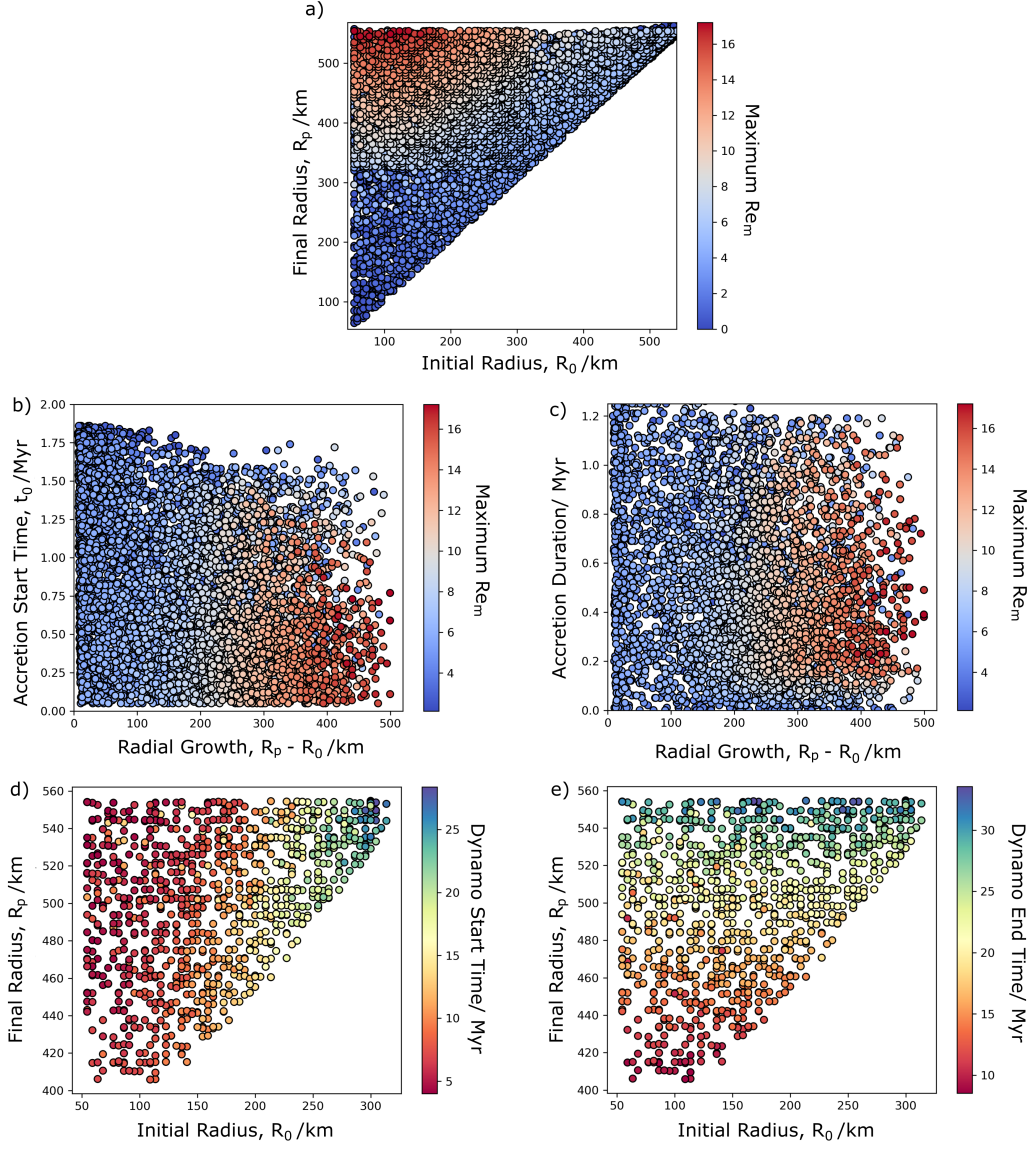


Figure 8. Model results of parameter sweep for silicate thermal diffusivity of $\kappa = 9 \times 10^{-7} \text{ m}^2 \text{ s}^{-1}$: a) Dependence of magnetic Reynolds number Re_m on initial and final planetary radius, b) accretion start time and c) accretion duration requirements for dynamo generation in bodies with core radii greater than 205 km. d) Start time and e) end time of dynamo generation as a function of initial and final radius.

Thermal Diffusivity, $\kappa_m / \text{m}^2 \text{s}^{-1}$	t_0 / Myr	$\Delta t_{acc} / \text{Myr}$	R_0 / km	R_p / km	ΔR_{acc}	Dynamo start time/ Myr	Dynamo end time/ Myr
6×10^{-7}	< 1.4	0.1-1.15	< 340	> 430	> 270	4.5-27	9-30
9×10^{-7}	< 1.4	0.09-1.19	< 350	> 410	> 210	4-28	8.5-33
12×10^{-7}	< 1.5	0.07-1.20	< 380	> 395	> 250	4-29	8-34

Table 3. Summary of the requirements for thermal dynamo generation in planetesimals for the range of thermal diffusivities investigated.

The silicate thermal diffusivity controls how fast and how much heat is moved around the planetesimal therefore the higher κ_m models record earlier dynamo onset times with smaller critical core radii.

804 **3.2.2 Structure of Planetesimals**

805 Our model results in both fully differentiated planetesimals and completely undif-
 806 ferentiated ones, which never form a core as they accrete too late to contain sufficient ^{26}Al
 807 for widespread melting of the body. It also produces partially-differentiated body with
 808 a liquid core and metal-depleted mantle buried underneath an undifferentiated, chon-
 809 dritic lid (Figure 9). We find that for convection to start over any portion of a planetes-
 810 imal and the differentiation process to begin, the planetesimal needs to begin accreting
 811 before 1.8 Myr after CAI formation. Any body that starts accreting after 1.8 Myr af-
 812 ter CAI formation will not contain enough initial ^{26}Al to melt the original chondritic
 813 material and initiate differentiation. Fully differentiated bodies, which melt sufficiently
 814 to segregate all the iron present in the body into the core, are produced when the end
 815 of the addition of cold, chondritic material to the planetesimal’s surface occurs by 2-2.5
 816 Myr after CAI formation (depending on initial and final radii, this period can extend
 817 to 3-4 Myr after CAI formation). Lastly, if a planetesimal starts accreting early enough
 818 to differentiate but has a relatively late addition of ^{26}Al -depleted material to its surface,
 819 it will end up with a partially differentiated structure with an inner liquid core and magma
 820 ocean beneath a thick, porous chondritic lid as discussed in section 3.1.3. The percent-
 821 age of the planetesimal radius which remains undifferentiated in this case can be up to
 822 80% (Figure 9).

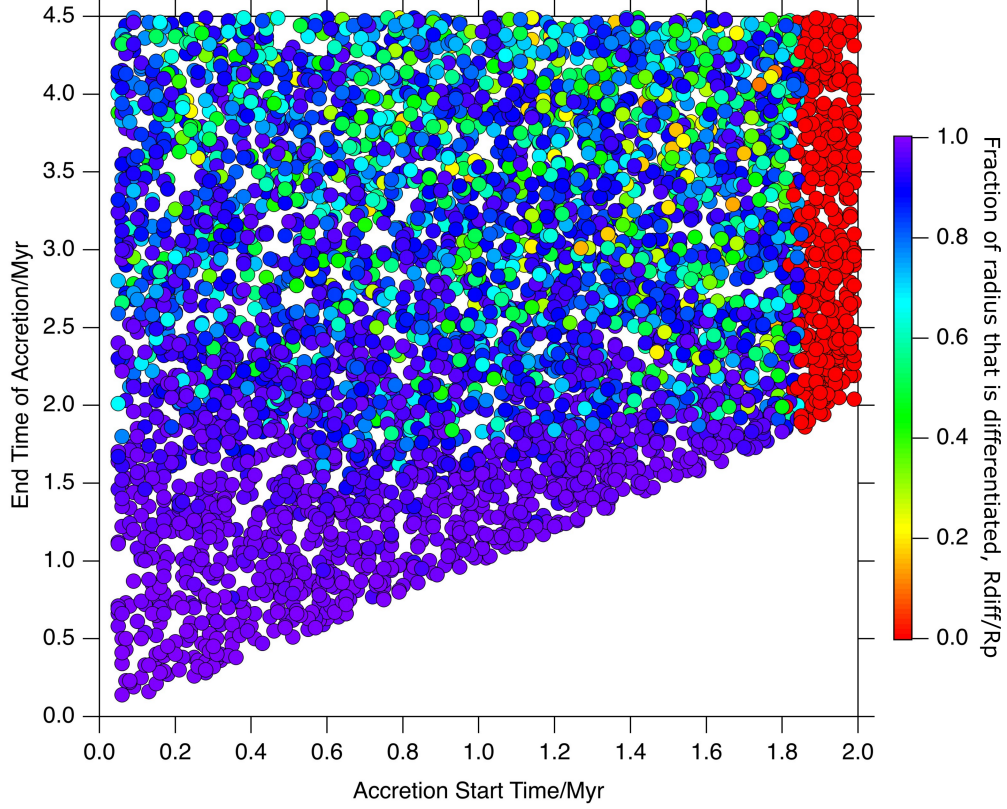


Figure 9. Dependence of the fraction of the planetesimal radius that differentiates as a function of accretion start time and duration. Bodies which start and finish accreting material to their surfaces before 2 Myr after CAI formation will result in fully differentiated bodies. Planetesimals which start accreting after 1.8 Myr after CAI formation will never differentiate. Partially differentiated bodies, in which between 20% and 100% of their final radii have undergone differentiation, are formed by accreting material continuously from both earlier and later than 1.8 Myr after CAI formation.

4 Discussion

4.1 Magnetic Epochs in Early Solar System

The timing and duration of the magnetic field generation by planetesimals during the early solar system reflect the accretionary history and structural evolution of the planetesimal and dictate whether a certain meteorite will have recorded a primary magnetic remanence. We find that internal dynamo field generation in planetesimals is not possible prior to at least 4 Myr post-CAI formation, consistent with the results of Bryson et al. (2019b), which have the earliest fields starting at 5 Myr after CAI formation. This is due to the radiogenic heating of the planetesimal’s silicate mantle by ^{26}Al which keeps the magma ocean at a higher temperature than the core for the first 3.5–4 Myr after CAI formation. Only once ^{26}Al has effectively decayed (i.e. > 4 Myr after CAI formation) can the magma ocean and subsequently the core start to cool and dynamo activity feasibly be generated. The earliest possible onset time for planetary magnetic fields of 4 Myr after CAI formation supports the nebula field origin for the magnetism recorded at 2–3 Myr after CAI formation by the chondrules in the Semarkona ordinary chondrite (Fu et al., 2014a) as this is the only viable long-lived magnetic field source during the first 4 Myr of the Solar System. The primary remanence in the CM chondrites (Cournède et al., 2015), the chondrules in both CR chondrites (Fu et al., 2020) and the CO chondrites (Borlina et al., 2020), and the ungrouped chondrite WIS 91600 (Bryson et al., 2020) has also been attributed to this early nebula field. Additionally, the R chondrites reportedly experienced a $\sim 5\mu\text{T}$ magnetic field at 4 Myr after CAI formation, which (Cournède et al., 2020) attribute possibly to an internal dynamo field on the R chondrite parent body. However, the ± 17 Myr uncertainty on the age of the remanence-carrying mineral phases in the R chondrites means a nebular origin for this magnetising field cannot be completely ruled out (Cournède et al., 2020). The nebula field had dissipated by 3.8–4.8 Myr after CAI formation (Wang et al., 2017) therefore any long-lived magnetic field recorded after this time is likely due to an internal dynamo on the meteorite’s parent body. The solar wind and impact-generated fields have been suggested as field sources for the primary remanence in meteorites. However, the intensity of the solar wind in the planet-forming regions of the solar system is $> 10^3$ times smaller than the paleointensities recovered from the meteorites (Oran et al., 2018), which is on the order of 1–10s μT . Magnetic fields generated during planetesimal impacts were transient and dissipated quickly over a timescale of 100–1000s (Hood & Artemieva, 2008), which contrasts with the slower

cooling rates (or aqueous alteration rates) experienced by these meteorites. Therefore, internally generated dynamo fields on the meteorite parent bodies are the most likely source for the primary remanences in meteorites recorded after 4 Myr after CAI formation. These dynamo fields could either have been thermally driven or compositionally driven during core crystallisation, depending critically on the time at which the remanence was recorded.

Our results indicate that dynamo generation by thermal convection alone in planetesimal cores is possible if core convection occurs over a distance of greater than 200 km and the core is cooling at a rate of $> 2 \text{ K Myr}^{-1}$. This is consistent with the required cooling rates and core sizes calculated by Nimmo (2009). Our lower bound on the core radius of 200 km is larger than that found by Bryson et al. (2019b), which requires $R_c > 160 \text{ km}$ for thermally driven dynamo generation. This is due to different formulation of the CMB heat flux during core cooling where, for the same CMB temperature difference, the CMB heat flux in the current study is lower than that used by Bryson et al. (2019b) (and Sterenborg and Crowley (2013)). In these other two models, the CMB heat flux is a fraction of the surface heat flux and is therefore dependent on the temperature difference between the magma ocean and the surface. Instead, we have assumed flux continuity across the CMB which results in more realistic but lower CMB heat fluxes throughout the planetesimals' evolution. Thus, we require larger core sizes to reach supercritical magnetic Reynold numbers in the current study.

Our size and cooling rate requirements place constraints on the accretionary history of planetesimals. For instance, we find our model requires that planetesimals grow by $> 250 \text{ km}$ in radius of the planetesimal from an initial radius to a final radius of $> 400 \text{ km}$ over a duration of greater than 100 kyr. This leads to gradual differentiation and core formation with duration on the order of 1 Myr that avoids the development of a strongly stably stratified layer at the top of the planetesimal's core and promotes early onset of whole core convection whilst the magma ocean is cooling quickly, generating supercritical magnetic Reynolds numbers. These results potentially allow us to use the timing and duration of these early thermal dynamo fields recorded by meteorites to recover information about the timescale of accretion of their parent bodies.

These results are in contrast to the conclusion of Bryson et al. (2019b) whose model can generate thermally driven dynamos for bodies that accreted instantaneously. The

difference in the two studies is due to the realistic inclusion of thermal stratifications in the core in the current model and points to the importance of the core thermal structure in determining the evolution of magnetic field generation in planetesimals. During the period of magma ocean superheating in Bryson et al. (2019b), the energy supplied to the core by the magma ocean is distributed homogeneously throughout the core, leading to an isothermal temperature profile throughout the core. Therefore, once the magma ocean becomes cooler than the top of the core, the whole core can convect immediately. These authors approximate the delay to full core convection due to the need to remove some stable stratification from the top of the core by maintaining a temporally isothermal core while heat production balances heat loss in the magma ocean. This approximates the time at which all the heat added to the core during the first 3 Myr (as a stably stratified layer) has been removed by whole core cooling. However, their formulation of the CMB heat flux as a fraction of the surface heat flux leads to $> 10 \text{ mW m}^{-2}$ CMB heat fluxes during this period of rapid magma ocean cooling and much faster removal of this stratification than in our model (which has CMB heat fluxes of $< 3 \text{ mW m}^{-2}$ during this period). The early removal of this stratification leads to whole core convection whilst the magma ocean is cooling quickly and the generation of supercritical magnetic Reynolds numbers at this time for bodies with core radii $> 160 \text{ km}$. In contrast, we treat the development and decay of the stable stratification as a diffusive problem with a subsequently slower heat transfer. This leads to more realistic and potentially much longer delays ($> 10\text{--}15 \text{ Myr}$) in whole core convection that only occurs once the magma ocean is cold and viscous in our instantaneously accreting bodies.

The time at which the thermally driven dynamo field shuts off depends solely on the final radius of the planetesimal as this controls how fast the body cools. The latest time we find thermally driven dynamo activity in planetesimals is 34 Myr after CAI formation for a body of 550 km in radius. The end times we find are later on the whole than those found by Bryson et al. (2019b). This is because our CMB heat fluxes are lower throughout the core cooling period therefore we can extract the same amount of heat from the core whilst keeping the CMB heat flux supercritical for a longer time than Bryson et al. (2019b).

Any long-lived magnetic fields generated after 34 Myr after CAI formation are therefore very likely driven by compositional convection during the crystallisation of the planetesimal's core. Exactly how small planetary cores crystallise is not well understood (Williams,

2009) but it is possible that low internal pressures lead to crystallisation starting at the CMB, followed by inward solidification of the core. Therefore dynamo generation during this period could be either iron-snow like (e.g. as in Ganymede, Rückriemen et al. (2015)) or driven by large-scale delamination of iron dendrites (e.g. as in Neufeld et al. (2019)). Both of these mechanisms are capable of producing buoyancy fluxes strong enough to drive dynamo fields. The timing and duration of these solidification-driven fields depends on the light element concentration, likely the sulfur content, of the core as this controls the core's liquidus temperature (and density contrast during core solidification). Our model assumes an Fe-FeS eutectic composition (32 wt % S) core composition which has a freezing temperature of 1234 K. In this case, core solidification starts tens of million years after cessation of convection in the magma ocean and any compositionally driven dynamo field is late. However, the observed sulfur concentration range across the magmatic iron meteorite groups is 0–18 wt % S (Goldstein et al., 2009). This range is inferred from the trace element content of the meteorites, which is sensitive to volatile loss during large impacts, and therefore might not reflect the original sulfur content of these parent body cores. Assuming that there has been no impact processing of these meteorites, the range of 0–18 wt % S corresponds to liquidus temperature range of 1486–1810 K. These liquidus temperatures are well within the range of core temperatures during the convecting magma ocean phase. Therefore it is possible for core solidification to have started before convection in the magma ocean ceases. As a result, we infer that magnetic fields generated prior to 34 Myr after CAI formation may not be due uniquely to thermal convection alone. The start of core crystallisation is likely reflected by an increase in the strength of recovered dipole field as the density difference induced during core solidification is orders of magnitude greater than that typically created during core cooling. For instance, such an increase in axial dipole moment of the geodynamo in the Ediacaran was used by Bono et al. (2019) to explore the timing of the nucleation of Earth's inner core. However, no meteorite group currently has sufficiently well-resolved time series of these early fields to distinguish between a thermally and compositionally driven field.

Our model assumption of a eutectic Fe-FeS composition for the metal in these bodies neglects the potential for an evolving core sulfur composition during core formation. This has two consequences for the timing and duration of magnetic fields in planetary cores. Firstly, it may affect the survival of thermal stratification in the core. In all

cases, the temperature at which the bodies first differentiate is less than the peak temperature of ~ 1625 K reached in the magma ocean. Therefore for iron-rich metal compositions, the metal melt that exists at the onset of core formation will be relatively enriched in sulfur compared to the bulk metal composition. This sulfur-rich melt will form the cool interior of the core. As the magma ocean then heats up due to the continued decay of ^{26}Al , it is likely that any new metal melt will be relatively iron-rich and thus more dense than the sulfur-rich proto-core. Therefore this iron-rich material will sink to the centre of the core, despite being warmer than the pre-existing core material, and any thermal stratification will be destroyed. This would then promote an early onset of whole core convection and thermally driven dynamo generation. Exactly how the sulfur content of the core forming metal melts evolves will also depend on the oxygen fugacity and silicate composition of the planetesimals as these factors control the partitioning of sulfur between the metal and silicate phases present. Secondly, as discussed above, the final core composition dictates the core liquidus temperature and thus the timing at which any compositional dynamo may start. As such, the evolution of the sulfur composition of the core could have an impact on the timings of both thermal convection and compositional convection. While we have neglected the possibility of compositional dynamos here, this work improves on our understanding on the controls of the timing and duration of thermally driven dynamo fields in planetesimals. In particular, our results provide a new constraint of 100–1000kyr on the timescale of planetesimal accretion required for the generation of thermally driven dynamo activity.

4.2 Properties of the Angrite Parent Body

The angrites are a well-studied group of rocky achondrites that are products of basaltic volcanic and plutonic activity on their differentiated parent body during the first few 10s Myr of the Solar System (Keil, 2012). The volcanic angrites formed 3.8 – 4.8 Myr after CAI formation (Keil (2012) and McKibbin et al. (2015)) and the more slowly-cooled plutonic angrites formed at approximately 11 Myr after CAI formation (Amelin, 2008). The volcanic angrites experienced a magnetic field of $< 0.6\mu\text{T}$ at 3.8 – 4.8 Myr after CAI formation (Wang et al., 2017), which has been interpreted as the absence of both the solar nebula field and any internally generated dynamo field. However, the plutonic angrite Angra dos Reis recorded a field of approximately $17\mu\text{T}$ at 11 Myr after CAI formation (Wang et al., 2017). Assuming that this was a thermally driven dynamo field, we can use our model results to constrain the accretional history of the angrite parent body, given a silicate thermal diffusivity of $\kappa_m = 9 \times 10^{-7} \text{ m}^2 \text{ s}^{-1}$. We take the window for the start time of this dynamo field as some time between 3.8–11 Myr after CAI formation and its end time as > 11 Myr. These constraints on start time and end time of dynamo activity require that the angrite parent body grew from an initial size of $R_0 < 225 \text{ km}$ to a final size of $R_p > 415 \text{ km}$ (figure 10) where the timescale of accretion (between 100–1200kyr) will depend on the exact final and initial radii. This is similar to the size constraint obtained by Bryson et al. (2019b). The planetesimal must also have grown by a minimum of 260 km during its accretionary phase, which needed to last $> 100 \text{ kyr}$, and reached its final size within the first 1.8 Myr in order to fully differentiate. These size requirements for the angrite parent body are consistent with the independent estimate of its radius of $R_p > 270 \text{ km}$ from the volatile contents of melt inclusions by Sarafian et al. (2017).

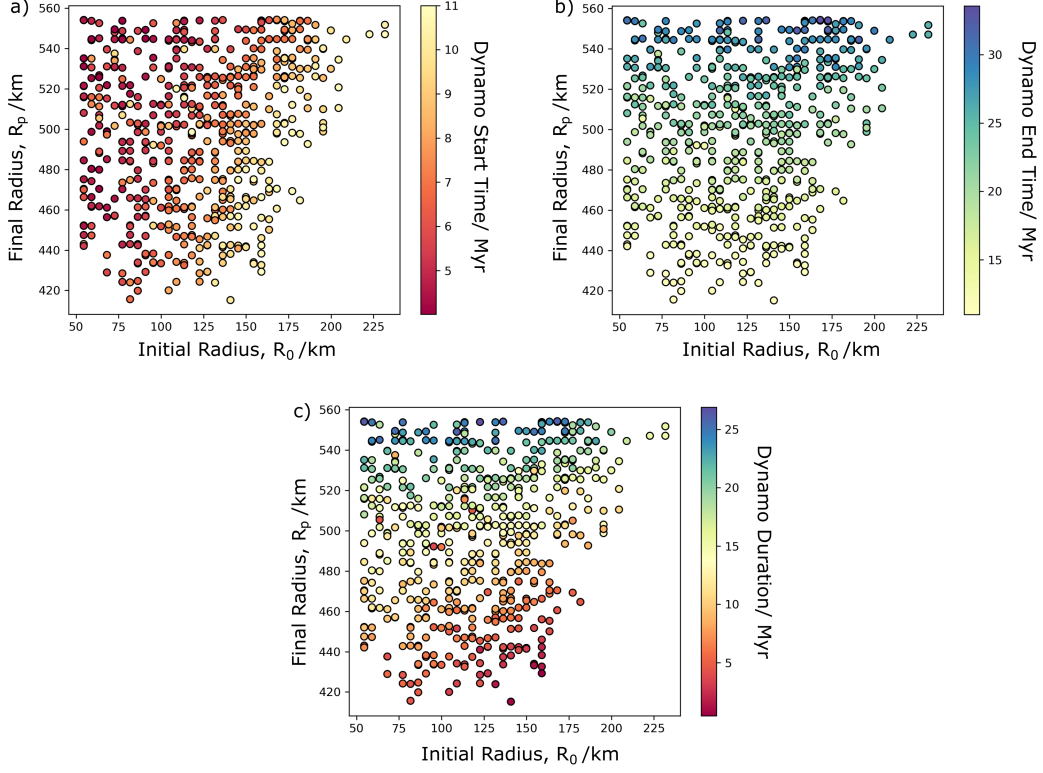


Figure 10. Dependence of a) the start time, b) the end time and c) the duration of the angrite thermal dynamo on initial and final planetary radii with an assumed silicate thermal diffusivity of $\kappa_m = 9 \times 10^{-7} \text{ m}^2 \text{ s}^{-1}$. Only model runs which resulted in dynamo generation starting some time between 3.8 – 11 Myr after CAI formation and ending after 11 Myr after CAI formation are shown here. A start time of 3.8 – 11 Myr after CAI formation requires an initial radius of < 225 km and a final radius of > 420 km is needed for the angrite parent body to still have a dynamo field at 11 Myr. The longevity of this dynamo field can range from a few Myr to > 20 Myr, depending on the exact values of the initial and final radii.

999

4.3 Structural Evolution of Planetesimals

1000

1001

1002

1003

1004

1005

1006

1007

1008

1009

1010

1011

1012

1013

1014

1015

1016

1017

1018

1019

1020

1021

1022

Our models produce a spectrum of planetesimals, from undifferentiated chondritic bodies through partially differentiated bodies with an unmelted lid atop a molten interior to fully differentiated achondrite-like bodies. In order for a planetesimal to form a core, it must accrete to a size of 70 km by 1.8 Myr after CAI formation. Otherwise, the concentration of ^{26}Al in the body is too low to drive the onset of convection and differentiation and the planetesimal remains a homogeneous mixture of metal and silicates. This is assuming that metal-silicate segregation by percolation is unimportant to the core formation process. However, the maximum temperature reached by the very centre of these undifferentiated bodies can be above 1500 K with complete Fe-FeS melting and silicate melt fractions of 20 – 30wt %. Modelling by Neumann et al. (2012) shows that core formation by percolation of eutectic Fe – FeS liquid through a semi-molten non-convecting silicate mantle can occur on the short < 2 Myr timescales required by the Hf-W systematics (Kruijer et al., 2014). Much of the planetesimal (> 45 % vol, Table 9 in Neumann et al. (2012)) remains undifferentiated in this case. Additionally, the high $\delta^{56}\text{Fe}$ value measured in the ureilite meteorites is interpreted as evidence for the segregation of a S-rich metal melt in the ureilite parent body without any significant silicate melting (Barrat et al., 2015). Therefore, we do consider metal-silicate segregation by percolation in the absence of a convecting magma ocean as a viable core formation mechanism which could generate partially differentiated bodies. However, the lack of a convecting magma ocean reduces the early high surface heat loss from these planetesimal that is required to generate the $> 10 \text{ mW m}^{-2}$ CMB heat fluxes needed to drive a thermal dynamo. As such, planetesimals that form cores through this process are unlikely to be relevant to this study of thermal dynamo generation.

1023

1024

1025

1026

1027

1028

1029

1030

For full differentiation, the planetesimal needs to have finished accreting by 2 – 2.5 Myr after CAI formation. Due to our imposed surface temperature boundary condition, the top 1 – 2 km of our models never differentiate. This is not realistic and it is likely that bodies that reach such high melt fractions in their interiors experience surface volcanism. The angrite parent body is such an example. This asteroid experienced basaltic volcanism early in its evolution with the plutonic and volcanic angrites originating from the top 100m of its crust (Keil, 2012). However, the large temperature difference between the planetesimal’s interior and the cold vacuum of space should have

ensured a frozen stagnant lid at its surface through which magma could have erupted to the surface in conduits.

Partially differentiated planetesimals can form by accreting material to their surfaces later than 2 – 2.5 Myr after CAI formation. The fraction of their radii that differentiates depends on the proportion of the body that is added after 1.8 Myr compared to its initial seed radius. This is due to the exponential nature of our chosen accretion law, which leads to the addition of the majority of mass of the planetesimal occurring in the last few time steps of accretion. If this final addition occurs after 1.8 Myr after CAI formation, there will be little ^{26}Al available to drive differentiation and the body will preserve a thick chondritic crust above a convecting magma ocean and liquid core. This liquid core can potentially generate a dynamo field, either during core cooling or core crystallisation, which could be recorded during aqueous alteration or cooling of material in the chondritic crust. There is a growing catalogue of chondritic meteorites in which the source of their primary magnetic remanence has been attributed to an internally generated thermally driven dynamo field. These include the CV meteorites, Kaba (Gattacceca et al., 2016), Allende (Carporzen et al., 2011) and Vigarano (Shah et al., 2017), which obtained their primary remanence between 6 – 20 Myr after CAI formation. This remanence has been interpreted as evidence for an active dynamo field and thus a liquid core on a partially differentiated CV parent body. The R chondrites also experienced a $\sim 5\mu\text{T}$ field at 4 ± 17 Myr after CAI formation which has been attributed to an internal dynamo in the R parent body (Cournède et al., 2020) and would suggest that the R parent body was also partially differentiated. Bryson et al. (2019b) used these observations to constrain the CV parent body size $R_0 > 220$ km growing to $R_p > 270$ km later. Meteorites from the H chondrites (Bryson et al., 2019a), mantle-hosted IIE irons (Maurel et al., 2020) and L/LL chondrites (Shah et al., 2017) also experienced a planetary dynamo field but these fields were younger and post-dated any thermally driven dynamo fields. Therefore these meteorites likely experienced magnetic fields driven by core crystallisation on their parent bodies. There are also several magnetised chondrites (e.g. the CM chondrites (Cournède et al., 2015) and WIS 91600 (Bryson et al., 2020)) that were likely magnetised by the solar nebula field during the first 4 Myr after CAI formation.

However, the partially-differentiated bodies that formed in our parameter sweeps and that retain an appreciable thickness of undifferentiated material do not produce ther-

mal dynamo fields due to their small core sizes and reduced core cooling due to insulation from thick chondritic lids. The planetesimals that do produce an early thermally-driven field in our model have differentiated over 95% of their final planetary radii (Figure 11). This corresponds to a maximum of 20 km of chondritic crust preserved at the surface, much of which will have undergone some metal and silicate melting and may no longer retain its chondritic texture. This is a product of the exponential accretion law leading to a large addition of material in the final stages of radial growth of the planetesimal as well as the requirement of core radii of > 200 km for supercritical magnetic Reynolds number. As such, it appears that a different accretional regime is required to explain the magnetic remanence carried by the CV chondrites and potentially the R chondrites.

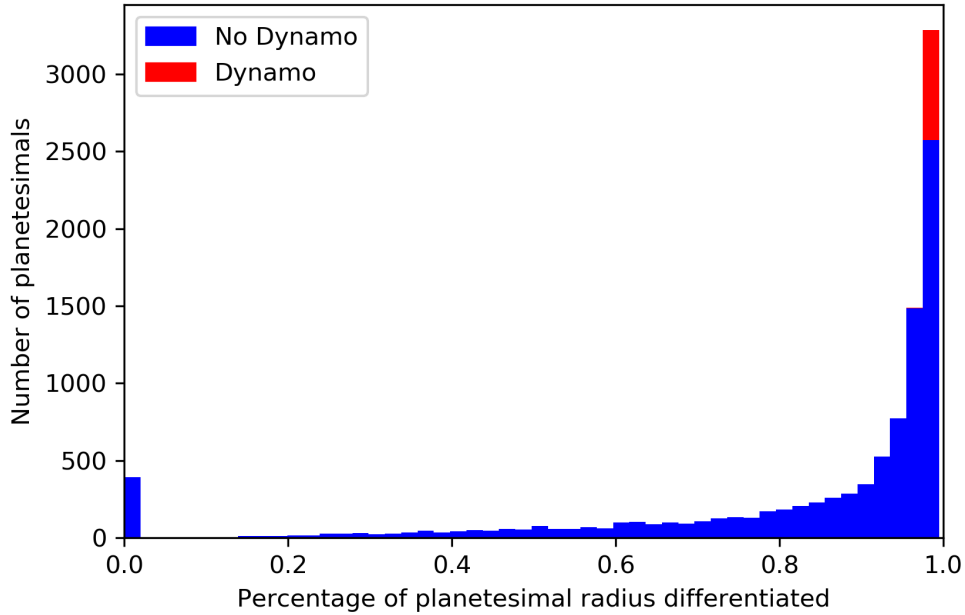


Figure 11. Histogram of the distribution of degrees of differentiation of planetesimals obtained acrossed both the wide and targeted parameter sweeps. The second targeted sweep has led to the bias in highly differentiated bodies as the start time of accretion was limited to the first 1.8 Myr of the Solar System during which time there was sufficient ^{26}Al to drive differentiation in any body > 70 km in radius.

5 Conclusions

- We have modelled planetesimal accretion and differentiation in order to investigate the effect of these processes on the ability of a planetesimal to generate dynamo activity by convection in their cores by cooling alone.
- The partitioning of ^{26}Al into the silicate magma ocean during differentiation leads to the development of a stably stratified layer in the core as the magma ocean continues to heat up. The depth and duration of initial core formation controls the size and strength of this stratification
- Quickly accreting planetesimals ($\Delta t_{\text{acc}} < 100$ kyr) form a large core very rapidly and the top of the core becomes strongly thermally stably stratified in the first 3–4 Myr after CAI formation by heating from the mantle above. This introduces a delay of > 10 Myr to the onset of whole core convection after the magma ocean starts to cool whilst this stable stratification is removed. By the time the whole core starts to convect, the magma ocean is cooling more slowly due to its increased viscosity, which results in subcritical values of the CMB heat flux.
- Planetesimals that accrete > 250 km of material to their surfaces over a timescale of > 100 kyr avoid developing this stable stratification below the CMB. Instead, this stratification is deep seated. Whole core convection can start earlier and coincide with the early period of fast magma ocean cooling whilst the magma ocean crystal fraction and viscosity are low. This can lead to the generation of thermal dynamo fields from 4–34 Myr after CAI formation in bodies with core sizes of greater than 200 km.
- Bodies that accrete slowly over > 1 Myr with significant addition of material to their surfaces after 1.8 Myr result in partially differentiated bodies with an unmelted chondritic lid atop a molten interior. However, none of these models generate a thermally driven dynamo due to their small relative core sizes and added insulation from the porous undifferentiated lids. Therefore, the paleomagnetic observations of thermal dynamos on partially differentiated bodies require a different accretionary regime, e.g., multistage accretion.
- Thermal dynamo generation is possible in planetesimals with core radii > 200 km that accrete over a timescale of 100–1200 kyr. The earliest possible onset time of these magnetic fields is 4–4.5 Myr after CAI formation, with the exact start time depending on the size and location of the stratification which develops dur-

1108 ing core formation. The end timing of these fields is controlled by the final plan-
 1109 etesimal radius with planetesimals of > 500 km in radius capable of generating
 1110 these fields until > 25 Myr after CAI formation.

- 1111 • We obtain constraints on the timing and duration of accretion of the angrite par-
 1112 ent body as well as its final size by comparing our model predictions to the mea-
 1113 sured paleomagnetic remanences in multiple angrites. In order to generate a ther-
 1114 mal dynamo at 11 Myr after CAI formation, the angrite parent body must have
 1115 finished accreting from an initial size of < 225 km to its full size of > 420 km
 1116 by 1.8 Myr after CAI formation. The duration of this accretion is between 90–
 1117 1190 kyr.

Acknowledgments

This work was funded by NERC grant number NE/L002507/1. J.F.J. Bryson would like to thanks St. John’s College, Cambridge for funding. No new experimental data was generated for this work. Data used in producing the figures in this work can be found in (Dodds et al., 2020).

References

- Amelin, Y. (2008). The U-Pb systematics of angrite sahara 99555. *Geochimica et Cosmochimica Acta*, 72(19), 4874–4885.
- Barrat, J.-A., Rouxel, O., Wang, K., Moynier, F., Yamaguchi, A., Bischoff, A., & Langlade, J. (2015). Early stages of core segregation recorded by Fe isotopes in an asteroidal mantle. *Earth and Planetary Science Letters*, 419, 93–100.
- Bono, R. K., Tarduno, J. A., Nimmo, F., & Cottrell, R. D. (2019). Young inner core inferred from Ediacaran ultra-low geomagnetic field intensity. *Nature Geoscience*, 12(2), 143–147.
- Borlina, C. S., Weiss, B. P., Bryson, J. F. J., & Lima, E. A. (2020). Measurements of solar nebula magnetic fields from CO chondrites. In *Lunar and planetary science conference* (p. 2283).
- Bryson, J. F. J., Neufeld, J. A., & Nimmo, F. (2019b). Constraints on asteroid magnetic field evolution and the radii of meteorite parent bodies from thermal modelling. *Earth and Planetary Science Letters*, 521, 68–78.
- Bryson, J. F. J., Nichols, C. I., Herrero-Albillos, J., Kronast, F., Kasama, T., Alimadadi, H., ... Harrison, R. J. (2015). Long-lived magnetism from solidification-driven convection on the pallasite parent body. *Nature*, 517(7535), 472.
- Bryson, J. F. J., Weiss, B., Getzin, B., Abrahams, J., Nimmo, F., & Scholl, A. (2019a). Paleomagnetic evidence for a partially differentiated ordinary chondrite parent asteroid. *Journal of Geophysical Research: Planets*, 124(7), 1880–1898.
- Bryson, J. F. J., Weiss, B. P., Lima, E. A., Gattacceca, J., & Cassata, W. S. (2020). Evidence for asteroid scattering and distal solar system solids from meteorite paleomagnetism. *The Astrophysical Journal*, 892(2), 126. doi: 10.3847/1538-4357/ab7cd4

- 1150 Carporzen, L., Weiss, B. P., Elkins-Tanton, L. T., Shuster, D. L., Ebel, D., & Gat-
 1151 tacceca, J. (2011). Magnetic evidence for a partially differentiated carbona-
 1152 ceous chondrite parent body. *Proceedings of the National Academy of Sciences*,
 1153 *108*(16), 6386–6389.
- 1154 Connelly, J. N., Bizzarro, M., Krot, A. N., Nordlund, Å., Wielandt, D., & Ivanova,
 1155 M. A. (2012). The absolute chronology and thermal processing of solids in the
 1156 solar protoplanetary disk. *Science*, *338*(6107), 651–655.
- 1157 Corrigan, C. M., Zolensky, M. E., Dahl, J., Long, M., Weir, J., Sapp, C., & Bur-
 1158 kett, P. J. (1997). The porosity and permeability of chondritic meteorites
 1159 and interplanetary dust particles. *Meteoritics & Planetary Science*, *32*(4),
 1160 509–515.
- 1161 Costa, A. (2005). Viscosity of high crystal content melts: dependence on solid frac-
 1162 tion. *Geophysical Research Letters*, *32*(22).
- 1163 Cournede, C., Gattacceca, J., Gounelle, M., Rochette, P., Weiss, B., & Zanda, B.
 1164 (2015). An early solar system magnetic field recorded in CM chondrites. *Earth*
 1165 *and Planetary Science Letters*, *410*, 62–74.
- 1166 Cournède, C., Gattacceca, J., Rochette, P., & Shuster, D. (2020). Paleomagnetism of
 1167 Rumuruti chondrites suggests a partially differentiated parent body. *Earth and*
 1168 *Planetary Science Letters*, *533*, 116042.
- 1169 de Wijs, G. A., Kresse, G., Vočadlo, L., Dobson, D., Alfe, D., Gillan, M. J., & Price,
 1170 G. D. (1998). The viscosity of liquid iron at the physical conditions of the
 1171 earth’s core. *Nature*, *392*(6678), 805–807.
- 1172 Dodds, K. H., Bryson, J. F., Neufeld, J. A., & Harrison, R. J. (2020). *Planetesimal*
 1173 *gradual accretion and thermal dynamo results*. doi: 10.5281/zenodo.4047972
- 1174 Doyle, P. M., Jogo, K., Nagashima, K., Krot, A. N., Wakita, S., Ciesla, F. J., &
 1175 Hutcheon, I. D. (2015). Early aqueous activity on the ordinary and carbona-
 1176 ceous chondrite parent bodies recorded by fayalite. *Nature Communications*,
 1177 *6*, 7444.
- 1178 Elkins-Tanton, L. T., Weiss, B. P., & Zuber, M. T. (2011). Chondrites as samples of
 1179 differentiated planetesimals. *Earth and Planetary Science Letters*, *305*(1-2), 1–
 1180 10.
- 1181 Fu, R., & Elkins-Tanton, L. T. (2014). The fate of magmas in planetesimals and the
 1182 retention of primitive chondritic crusts. *Earth and Planetary Science Letters*,

- 1183 390, 128–137.
- 1184 Fu, R., Kehayias, P., Weiss, B. P., Schrader, D. L., Bai, X.-N., & Simon, J. B.
 1185 (2020). Weak magnetic fields in the outer solar nebula recorded in CR chon-
 1186 drites. *Journal of Geophysical Research: Planets*, e2019JE006260.
- 1187 Fu, R., Lima, E., & Weiss, B. (2014b). No nebular magnetization in the Allende CV
 1188 carbonaceous chondrite. *Earth and Planetary Science Letters*, 404, 54–66.
- 1189 Fu, R., Weiss, B. P., Lima, E. A., Harrison, R. J., Bai, X.-N., Desch, S. J., ... others
 1190 (2014a). Solar nebula magnetic fields recorded in the Semarkona meteorite.
 1191 *Science*, 346(6213), 1089–1092.
- 1192 Fu, R., Weiss, B. P., Shuster, D. L., Gattacceca, J., Grove, T. L., Suavet, C., ...
 1193 Kuan, A. T. (2012). An ancient core dynamo in asteroid vesta. *Science*,
 1194 338(6104), 238–241.
- 1195 Gattacceca, J., Weiss, B. P., & Gounelle, M. (2016). New constraints on the mag-
 1196 netic history of the CV parent body and the solar nebula from the Kaba
 1197 meteorite. *Earth and Planetary Science Letters*, 455, 166–175.
- 1198 Goldstein, J., Scott, E., & Chabot, N. (2009). Iron meteorites: crystallization, ther-
 1199 mal history, parent bodies, and origin. *Chemie der Erde-Geochemistry*, 69(4),
 1200 293–325.
- 1201 Henke, S., Gail, H.-P., Tieloff, M., & Schwarz, W. (2013). Thermal evolution
 1202 model for the H chondrite asteroid-instantaneous formation versus protracted
 1203 accretion. *Icarus*, 226(1), 212–228.
- 1204 Holzheid, A., Schmitz, M. D., & Grove, T. L. (2000). Textural equilibria of iron
 1205 sulfide liquids in partly molten silicate aggregates and their relevance to core
 1206 formation scenarios. *Journal of Geophysical Research: Solid Earth*, 105(B6),
 1207 13555–13567.
- 1208 Hood, L. L., & Artemieva, N. A. (2008). Antipodal effects of lunar basin-forming
 1209 impacts: Initial 3d simulations and comparisons with observations. *Icarus*,
 1210 193(2), 485–502.
- 1211 Johansen, A., Mac Low, M.-M., Lacerda, P., & Bizzarro, M. (2015). Growth of
 1212 asteroids, planetary embryos, and Kuiper belt objects by chondrule accretion.
 1213 *Science Advances*, 1(3), e1500109.
- 1214 Kakar, A. K., & Chaklader, A. (1967). Deformation theory of hot-pressing. *Journal*
 1215 *of applied physics*, 38(8), 3223–3230.

- 1216 Keil, K. (2012). Angrites, a small but diverse suite of ancient, silica-undersaturated
 1217 volcanic-plutonic mafic meteorites, and the history of their parent asteroid.
 1218 *Geochemistry*, 72(3), 191–218.
- 1219 Krause, M., Henke, S., Gail, H. P., Tieloff, M., Blum, J., Skorov, Y. V., ... Kleine,
 1220 T. (2011, March). Modeling the early thermal evolution of meteorite parent
 1221 bodies based on new thermal conductivity measurements of highly porous
 1222 aggregates. In *Lunar and planetary science conference* (p. 2696).
- 1223 Kruijer, T., Sprung, P., Kleine, T., Leya, I., Burkhardt, C., & Wieler, R. (2012).
 1224 Hf-W chronometry of core formation in planetesimals inferred from weakly
 1225 irradiated iron meteorites. *Geochimica et Cosmochimica Acta*, 99, 287–304.
- 1226 Kruijer, T., Touboul, M., Fischer-Gödde, M., Bermingham, K., Walker, R., &
 1227 Kleine, T. (2014). Protracted core formation and rapid accretion of proto-
 1228 planets. *Science*, 344(6188), 1150–1154.
- 1229 Laporte, D., & Provost, A. (2000). The grain-scale distribution of silicate, carbon-
 1230 ate and metallosulfide partial melts: a review of theory and experiments. In
 1231 *Physics and chemistry of partially molten rocks* (pp. 93–140). Springer.
- 1232 Lichtenberg, T., Keller, T., Katz, R. F., Golabek, G. J., & Gerya, T. V. (2019).
 1233 Magma ascent in planetesimals: Control by grain size. *Earth and Planetary*
 1234 *Science Letters*, 507, 154–165.
- 1235 Maurel, C., Bryson, J. F., Lyons, R. J., Ball, M. R., Chopdekar, R. V., Scholl, A.,
 1236 ... Weiss, B. P. (2020). Meteorite evidence for partial differentiation and
 1237 protracted accretion of planetesimals. *Science Advances*, 6(30), eaba1303.
- 1238 Maurel, C., Bryson, J. F. J., Weiss, B. P., & Scholl, A. (2018). Paleomagnetic ev-
 1239 idence for a layered partially differentiated iron-meteorite parent body. *Lunar*
 1240 *and Planetary Science Conference*.
- 1241 McKibbin, S. J., Ireland, T. R., Amelin, Y., & Holden, P. (2015). Mn–Cr dating of
 1242 Fe- and Ca-rich olivine from ‘quenched’ and ‘plutonic’ angrite meteorites using
 1243 secondary ion mass spectrometry. *Geochimica et Cosmochimica Acta*, 157,
 1244 13–27.
- 1245 Merk, R., Breuer, D., & Spohn, T. (2002). Numerical modeling of ^{26}Al -induced ra-
 1246 dioactive melting of asteroids considering accretion. *Icarus*, 159(1), 183–191.
- 1247 Morard, G., Bouchet, J., Rivoldini, A., Antonangeli, D., Roberge, M., Boulard, E.,
 1248 ... Mezouar, M. (2018). Liquid properties in the Fe–FeS system under moder-

- 1249 ate pressure: tool box to model small planetary cores. *American Mineralogist:*
1250 *Journal of Earth and Planetary Materials*, 103(11), 1770–1779.
- 1251 Néri, A., Guignard, J., Monnereau, M., Toplis, M., & Quitté, G. (2019). Metal
1252 segregation in planetesimals: Constraints from experimentally determined
1253 interfacial energies. *Earth and Planetary Science Letters*, 518, 40–52.
- 1254 Neufeld, J. A., Bryson, J. F. J., & Nimmo, F. (2019). The top-down solidification
1255 of iron asteroids driving dynamo evolution. *Journal of Geophysical Research:*
1256 *Planets*.
- 1257 Neumann, W., Breuer, D., & Spohn, T. (2012). Differentiation and core formation in
1258 accreting planetesimals. *Astronomy & Astrophysics*, 543, A141.
- 1259 Neumann, W., Breuer, D., & Spohn, T. (2014). Differentiation of Vesta: Impli-
1260 cations for a shallow magma ocean. *Earth and Planetary Science Letters*, 395,
1261 267–280.
- 1262 Nichols, C. I., Bryson, J. F. J., Herrero-Albillos, J., Kronast, F., Nimmo, F., & Har-
1263 rison, R. J. (2016). Pallasite paleomagnetism: Quiescence of a core dynamo.
1264 *Earth and Planetary Science Letters*, 441, 103–112.
- 1265 Nimmo, F. (2009). Energetics of asteroid dynamos and the role of compositional
1266 convection. *Geophysical Research Letters*, 36(10).
- 1267 Olson, P., & Christensen, U. R. (2006). Dipole moment scaling for convection-driven
1268 planetary dynamos. *Earth and Planetary Science Letters*, 250(3-4), 561–571.
- 1269 Opeil, C., Consolmagno, G., & Britt, D. (2010). The thermal conductivity of mete-
1270 orites: New measurements and analysis. *Icarus*, 208(1), 449–454.
- 1271 Opeil SJ, C., Consolmagno SJ, G., Safarik, D., & Britt, D. (2012). Stony meteorite
1272 thermal properties and their relationship with meteorite chemical and physical
1273 states. *Meteoritics & Planetary Science*, 47(3), 319–329.
- 1274 Oran, R., Weiss, B. P., & Cohen, O. (2018). Were chondrites magnetized by the
1275 early solar wind? *Earth and Planetary Science Letters*, 492, 222–231.
- 1276 Rao, A., & Chaklader, A. (1972). Plastic flow during hot-pressing. *Journal of the*
1277 *American ceramic society*, 55(12), 596–601.
- 1278 Robuchon, G., & Nimmo, F. (2011). Thermal evolution of Pluto and implications for
1279 surface tectonics and a subsurface ocean. *Icarus*, 216(2), 426–439.
- 1280 Rückriemen, T., Breuer, D., & Spohn, T. (2015). The Fe snow regime in
1281 Ganymede’s core: A deep-seated dynamo below a stable snow zone. *Jour-*

- 1282 *nal of Geophysical Research: Planets*, 120(6), 1095–1118.
- 1283 Sarafian, A. R., Hauri, E. H., McCubbin, F. M., Lapen, T. J., Berger, E. L., Nielsen,
1284 S. G., ... Sarafian, E. (2017). Early accretion of water and volatile elements
1285 to the inner solar system: evidence from angrites. *Philosophical Transactions*
1286 *of the Royal Society A: Mathematical, Physical and Engineering Sciences*,
1287 375(2094), 20160209.
- 1288 Scheinberg, A., Elkins-Tanton, L., Schubert, G., & Bercovici, D. (2016). Core solid-
1289 ification and dynamo evolution in a mantle-stripped planetesimal. *Journal of*
1290 *Geophysical Research: Planets*, 121(1), 2–20.
- 1291 Schwenn, M. B., & Goetze, C. (1978). Creep of olivine during hot-pressing. *Tectono-*
1292 *physics*, 48(1-2), 41–60.
- 1293 Shah, J., Bates, H. C., Muxworthy, A. R., Hezel, D. C., Russell, S. S., & Genge,
1294 M. J. (2017). Long-lived magnetism on chondrite parent bodies. *Earth and*
1295 *Planetary Science Letters*, 475, 106–118.
- 1296 Shannon, M., & Agee, C. (1996). High pressure constraints on percolative core for-
1297 mation. *Geophysical Research Letters*, 23(20), 2717–2720.
- 1298 Solomatov, V. (1995). Scaling of temperature-and stress-dependent viscosity convec-
1299 tion. *Physics of Fluids*, 7(2), 266–274.
- 1300 Sterenborg, M. G., & Crowley, J. W. (2013). Thermal evolution of early solar sys-
1301 tem planetesimals and the possibility of sustained dynamos. *Physics of the*
1302 *Earth and Planetary Interiors*, 214, 53–73.
- 1303 Wang, H., Weiss, B. P., Bai, X.-N., Downey, B. G., Wang, J., Wang, J., ... Zu-
1304 colotto, M. E. (2017). Lifetime of the solar nebula constrained by meteorite
1305 paleomagnetism. *Science*, 355(6325), 623–627.
- 1306 Warren, P. H. (2001). Porosities of lunar meteorites: Strength, porosity, and petro-
1307 logic screening during the meteorite delivery process. *Journal of Geophysical*
1308 *Research: Planets*, 106(E5), 10101–10111. doi: 10.1029/2000JE001283
- 1309 Warren, P. H. (2011). Ejecta–megaregolith accumulation on planetesimals and large
1310 asteroids. *Meteoritics & Planetary Science*, 46(1), 53–78.
- 1311 Weiss, B. P., Gattacceca, J., Stanley, S., Rochette, P., & Christensen, U. R. (2010).
1312 Paleomagnetic records of meteorites and early planetesimal differentiation.
1313 *Space Science Reviews*, 152(1-4), 341–390.
- 1314 Weiss, B. P., Wang, H., Sharp, T. G., Gattacceca, J., Shuster, D. L., Downey, B., ...

- 1315 others (2017). A nonmagnetic differentiated early planetary body. *Earth and*
1316 *Planetary Science Letters*, 468, 119–132.
- 1317 Williams, Q. (2009). Bottom-up versus top-down solidification of the cores of small
1318 solar system bodies: Constraints on paradoxical cores. *Earth and Planetary*
1319 *Science Letters*, 284(3-4), 564–569.
- 1320 Wilson, L., & Keil, K. (2017). Arguments for the non-existence of magma oceans in
1321 asteroids. In *Planetesimals: Early differentiation and consequences for planets*
1322 (pp. 159–179). Cambridge University Press.
- 1323 Yomogida, K., & Matsui, T. (1984). Multiple parent bodies of ordinary chondrites.
1324 *Earth and Planetary Science Letters*, 68(1), 34–42.